

A sample of mJy radio sources at 1.4 GHz in the Lynx and Hercules fields - II. Cosmic evolution of the space density of FRI radio sources

E. E. Rigby^{1,2*}, P. N. Best² I. A. G. Snellen³

¹ School of Physics and Astronomy, Cardiff University, 5 The Parade, Cardiff CF24 3YB

²SUPA†, University of Edinburgh, Institute for Astronomy, Royal Observatory, Edinburgh EH9 3HJ, UK

³Leiden Observatory, Leiden University, Niels Bohrweg 2, NL-2300RA Leiden, The Netherlands

25 October 2018

ABSTRACT

In this paper the cosmic evolution of the space density of Fanaroff & Riley Class I (FRI) radio sources is investigated out to $z \sim 1$, in order to understand the origin of the differences between these and the more powerful FRIIs. High resolution radio images are presented of the best high redshift FRI candidate galaxies, drawn from two fields of the Leiden Berkeley Deep Survey, and previously defined in Rigby, Snellen & Best (2007, Paper I). Together with lower resolution radio observations (both previously published in Paper I and, for a subset of sources, also presented here) these are used to morphologically classify the sample. Sources which are clearly resolved are classified by morphology alone, whereas barely or unresolved sources were classified using a combination of morphology and flux density loss in the higher resolution data, indicative of resolved out extended emission. The space densities of the FRIs are then calculated as a function of redshift, and compared to both measurements of the local value and the behaviour of the more powerful FRIIs. The space density of FRI radio sources with luminosities (at 1.4 GHz) $> 10^{25}$ W/Hz is enhanced by a factor of 5–9 by $z \sim 1$, implying moderately strong evolution of this population; this enhancement is in good agreement with models of FRII evolution at the same luminosity. There are also indications that the evolution is luminosity dependent, with the lower powered sources evolving less strongly.

Key words: galaxies: active – galaxies: evolution – radio continuum: galaxies

1 INTRODUCTION

It has been known for some time that powerful ($P_{178\text{MHz}} > 10^{24-25} \text{ WHz}^{-1}\text{sr}^{-1}$) radio galaxies undergo strong cosmic evolution, with density enhancements, over the local value, ranging from ~ 10 , to 100–1000 for the most luminous sources at redshifts 1–2 (e.g. Wall et al. (1980)). These results were supported by Dunlop & Peacock (1990, hereafter DP90) who found that including a high luminosity, strongly evolving population in their modelling of the radio luminosity function fitted the data well.

The increased difficulty in detecting lower powered radio galaxies over comparable distances means that their evolutionary behaviour is less clear. Initial, low redshift studies, suggested that they had a constant space density (e.g. Jackson & Wall (1999)) and this was subsequently supported at higher redshift by Clewley & Jarvis (2004). However, DP90 found that their models were better fit if the low luminosity population was weakly evolving, and Sadler et al. (2007), using a sample selected in a similar way to that of Clewley & Jarvis, found that the no-evolution scenario is ruled out at a significance level of $> 6\sigma$. Additionally, Willott et al.

(2001), also see evolution in their low luminosity, weak emission line, population.

This high/low power radio galaxy split corresponds to the division between Fanaroff & Riley Class I and II sources (FRI and FRII; Fanaroff & Riley, 1974). Of the two types, FRIIs are the more powerful, but it should be noted that there is significant overlap at the break luminosity. The bulk of the emission in FRIIs originates from the hotspots at the ends of their highly collimated, ‘edge-brightened’, jets. FRIs, on the other hand, typically have ‘edge-darkened’ jets which are brighter towards their central regions and which also tend to flare out close to the nucleus. It is not yet clear whether the differences between the two classes arise from fundamental differences in their central engines (e.g. advection dominated accretion flow in FRIs arising from a lower accretion rate) as argued by e.g. Baum, Zirbel & O’Dea (1995), or whether it is the environments in which the jets of these objects reside which determines their observed properties (e.g. Gopal-Krishna & Wiita (2000) and Gawroński et al. (2006)), or even some combination of the two.

An important tool, therefore, for investigating the morphological differences between the two FR classes comes from measurements of their cosmic evolution. Since the FRI/FRII break luminosity is not fixed, but is a function of host galaxy magnitude

* E-mail:Emma.Rigby@astro.cf.ac.uk

† Scottish Universities Physics Alliance

(Ledlow & Owen 1996), morphological classification of the radio galaxies in a sample is a necessity if an accurate picture of the cosmic evolution of FRIs is to be obtained. Any similarities detected in the variation of FRIs and FRIIs over cosmic time lends weight to the extrinsic, environmental, model since objects with similar underlying properties, at the same luminosity, would be expected to evolve similarly as well. If this is the case, then it implies that FRIs and FRIIs may simply represent different stages in the evolution of a radio galaxy, which, in this scenario, would start as a high luminosity FRII with powerful jets, which then weakens and dims over time (e.g. Willott et al. (2001); Kaiser & Best (2007)).

In addition to clarifying the FRI/II differences, the cosmic evolution of FRIs in particular may also be important for galaxy formation and evolution models, which are increasingly using radio galaxies to provide the feedback necessary to halt the problem of massive galaxy overgrowth (e.g. Bower et al. 2006). Best et al., (2006) suggest that it is the lower luminosity sources, perhaps the FRI population alone, that are mainly responsible for this. Understanding their behaviour may therefore provide the key to understanding this mechanism as well.

Snellen & Best (2001) made a first attempt at determining the space density of morphologically classified FRIs, using the two $z > 1$ FRIs detected in the Hubble Deep and Flanking Fields (HDF+FF) area. The small number of sources meant that a direct calculation would have been unreliable, but they were able to show that the probability of detecting these two FRIs if the population undergoes no evolution was $< 1\%$, and was instead consistent with a space density enhancement comparable to that of less luminous FRII galaxies at the same redshift. More recently, Jamrozy (2004), using the number counts of two complete, morphologically classified, radio samples, also found that a positive cosmic evolution for the most luminous FRI sources is needed to fit their observational data out to $z \sim 2$.

The aim of this work is to improve on the results of these previous analyses using a deep, wide field, 1.4 GHz, Very Large Array (VLA) A–array survey, an order of magnitude larger than the HDF+FF; this area is large enough to allow the space density to be directly measured for the first time. The survey was split over two fields of 0.29 sq. degrees each – one in the constellation of Lynx at right ascension, $\alpha = 8h45$, declination, $\delta = +44.6^\circ$ (J2000) and one in Hercules at $\alpha = 17h20$, $\delta = +49.9^\circ$ (J2000) – which were originally observed as part of the Leiden–Berkeley Deep Survey (LBDS; Kron, 1980; Koo & Kron, 1982). These fields are ideal for this work due to the existence of previous low resolution (12.5'') radio observations (Windhorst et al. 1984; Oort & Windhorst 1985; Oort & van Langevelde 1987). These can be used, in conjunction with higher resolution data, to look for flux density losses in the sample, which in turn can be used for FRI classification (see §4 for full details). Alongside this, the Hercules field has some previous optical and spectroscopic observations by Waddington et al., (2000), whilst the Lynx field is also covered by the Sloan Digital Sky Survey (York et al. 2000; Stoughton et al. 2002).

The survey consists of a complete sample of 81 radio sources, evenly spread over the two fields, all above the limiting flux density, $S_{1.4\text{GHz}}$, of 0.5 mJy in the A–array radio data. Optical and infra-red observations with the Isaac Newton Telescope (INT) and the UK Infra-red Telescope (UKIRT) respectively, resulted in a host–galaxy identification fraction of 85%, with 12 sources remaining unidentified at a level of $r' \geq 25.2$ mag (Hercules; 4 sources) or $r' \geq 24.4$ mag (Lynx; 7 sources) or $K \geq 20$ mag. New spectroscopic data obtained with the Telescopio Nazionale Galileo (TNG), combined with previously published results meant that the redshift

completeness was 49%. The redshifts for the remaining sources with a host galaxy detection were estimated using either the $K-z$ or $r-z$ magnitude–redshift relations (Willott et al. 2003; Snellen et al. 1996). Full details of the observations used to define the sample, and the resulting 1.4 GHz flux densities, magnitudes and redshifts, can be found in Rigby, Snellen & Best (2007, hereafter Paper I).

In this paper we present the additional radio observations, both low and high resolution, along with the FRI source classification and space density measurements. The layout of the paper is as follows: Section 2 describes the low resolution VLA B–array observations of the Lynx field; Section 3 then describes the high redshift FRI candidate selection and their high resolution radio follow–up. Section 4 outlines the method used to classify the sample and Section 5 then describes the steps taken to measure the space density of the identified FRIs. Finally Section 6 discusses the results and presents the conclusions of this work. Throughout this paper values for the cosmological parameters of $H_0 = 71 \text{ km s}^{-1}\text{Mpc}^{-1}$, $\Omega_m = 0.27$ and $\Omega_\Lambda = 0.73$ are used.

2 LOW RESOLUTION LYNX FIELD RADIO OBSERVATIONS

The aim of the low–resolution Lynx field VLA B–array observations was to provide a measure of the total flux density for each field source, and to look for any extended emission that may have been resolved out in the 1.5'' resolution A–array data presented in Paper I. Complimentary observations of the Hercules field in this configuration were not done due to time constraints.

The observations took place on 30th October 2003, in L–band (1.4 GHz), using the wide–field mode. The flux, point and phase calibrators used were 3C286, 3C147 and 0828+493 respectively and the total exposure time on the field was 7000s; this was split into five periods which were interspersed with ~ 120 s visits to the phase calibrator. 8 channels, at frequencies of 1.474 and 1.391 GHz, with a total bandwidth of 25 MHz, were used, to minimise bandwidth smearing effects. Full polarization was observed.

The data were calibrated using the NRAO AIPS package. Since sources located at all positions in the final radio image need to be considered, the non–coplanar array wide–field imaging techniques, incorporated into the AIPS task IMAGR, were used. The field was split into facets, centred on the positions of each source from the A–array observations and the centre was shifted to the centre of each facet and imaged and deconvolved in turn. Each facet was 256 by 256 pixels (with 1.0'' per pixel).

The deconvolution and CLEANing of each facet was done using 5000 iterations and nearly natural weighting to minimise the noise in the resulting CLEAN image. No self–calibration was carried out due to the weakness of the sources. The final noise level reached for all the facets was $\sim 50 \mu\text{Jy/beam}$, with a resolution of 5.36'' by 4.67''. Finally a primary beam correction was applied to each image to account for the attenuation of the beam away from the pointing centre.

2.1 Source detection and flux density measurement

All the sources in the Lynx field complete sample were detected in these observations. Their flux densities were, as with the A–array data (see Paper I), measured with *tvstat* if they showed extension or with *imfit* if they appeared compact. The method used for each source in the complete sample, along with the resulting flux densities and primary beam correction factors, can be found in Table

Table 1. The primary-beam corrected flux densities for the (complete sample) Lynx field B-array observations along with the correction factors, C_{PB} , used. An *I* in the final column indicates an *imfit* measured flux density; a *T* indicates a *tvstat* measurement. A primary beam correction error of 20% of the difference between the corrected and un-corrected flux density has been incorporated into the quoted errors.

Name	$S_{1.4\text{GHz}}$ (mJy)	C_{PB}	Measure
55w116	2.05 ± 0.43	2.22	T
55w118	0.85 ± 0.13	1.92	I
55w120	1.91 ± 0.43	2.68	T
55w121	1.24 ± 0.14	1.60	I
55w122	0.76 ± 0.18	1.45	I
55w123	1.09 ± 0.14	1.33	I
55w124	2.58 ± 0.10	1.35	I
55w127	1.72 ± 0.11	1.36	I
55w128	4.10 ± 0.56	2.05	T
55w131	1.20 ± 0.20	1.48	T
55w132	1.83 ± 0.36	2.05	T
55w133	2.17 ± 0.13	1.47	I
55w135	2.61 ± 0.37	1.98	T
55w136	0.90 ± 0.11	1.10	I
55w137	1.70 ± 0.17	1.29	T
55w138	1.81 ± 0.12	1.37	I
55w140	0.58 ± 0.09	1.06	I
55w141	0.60 ± 0.60	1.19	I
55w143a	2.22 ± 0.11	1.34	I
55w143b	0.65 ± 0.17	1.33	I
55w147	2.24 ± 0.14	1.82	I
55w149	7.63 ± 1.14	3.20	T
55w150	0.60 ± 0.14	1.88	I
55w154	12.90 ± 0.44	1.13	T
55w155	1.63 ± 0.15	1.55	I
55w156	4.02 ± 0.26	1.19	T
55w157	1.61 ± 0.13	1.68	I
55w159a	6.61 ± 0.21	2.69	I
55w159b	1.08 ± 0.31	2.55	I
55w160	0.77 ± 0.09	1.32	I
55w161	0.87 ± 0.16	1.87	I
55w165a	17.51 ± 1.33	2.06	T
55w165b	1.40 ± 0.23	1.99	I
55w166	2.26 ± 0.17	2.07	I
60w016	0.57 ± 0.15	1.52	I
60w024	0.25 ± 0.08	1.29	I
60w032	0.29 ± 0.10	1.51	I
60w039	0.64 ± 0.15	1.38	I
60w055	0.80 ± 0.27	2.34	I
60w067	0.65 ± 0.11	1.70	I
60w071	0.59 ± 0.19	1.42	I
60w084	0.54 ± 0.16	2.08	I

1. The corresponding radio contour maps (without primary-beam corrections applied) can be found in Figure A1. The results for additional sources not in the complete sample can be found in Table 2 and Figure A2; these sources were excluded as they did not fall within the field of view of the optical imaging described in Paper I.

3 FRI CANDIDATE SELECTION AND HIGH RESOLUTION RADIO OBSERVATIONS

The high-resolution radio observations were, by necessity, limited to the best high-redshift FRI candidates only. The next step therefore, was to select these candidate sources from the sample. The candidate criteria were, firstly, that their redshifts (or estimated red-

Table 2. The primary-beam corrected flux densities for the sources not included in the Lynx complete sample, along with the correction factors, C_{PB} , used. An *I* in the final column indicates an *imfit* measured flux density; a *T* indicates a *tvstat* measurement. A primary beam correction error of 20% of the difference between the corrected and un-corrected flux density has been incorporated into the quoted errors.

Name	$S_{1.4\text{GHz}}$ (mJy)	C_{PB}	Measure
55w119	1.97 ± 0.36	3.86	I
55w125	18.87 ± 4.04	12.01	I
55w126	4.13 ± 0.90	6.37	I

shifts) were $\gtrsim 1.0$ and, secondly, that extended emission was visible in their radio image; this extension was defined, by inspection, as structure that deviated from a compact form. Since the high-resolution observations took place using two different instruments, the VLA+PieTown (VLA+Pt) link (§3.1) and the MERLIN (Multi Element Radio Linked Interferometer) array (§3.2), with slightly different characteristics, as described below, two different subsamples of these candidates were observed. Where possible, candidate sources were included in both observations to increase the possibility of detecting and classifying significant extended emission. Three of the high-redshift candidates were not able to be included in either observation due to time constraints; these were 53w081 in Hercules and 55w155 and 55w166 in Lynx.

3.1 VLA A+PieTown observations

The 27 radio antennae of the VLA can be linked with one of the antennas of the Very Long Baseline Array (VLBA), located 50 km away from the array centre at Pie Town. The extra baselines this adds means that the VLA+Pt can reach sub-arcsecond resolution at 1.4 GHz.

The candidate sources in the Hercules field, listed in Table 3, were individually observed on 26th September 2004 with the VLA+Pt at 1.4 GHz (L band). The candidate Lynx sources were observed similarly on 18th February 2006. 50 MHz channels at 1.385 and 1.465 GHz were used for both observations. The details of the exposure times for each source can be found in Table 3. The flux and point calibrator calibrator for both fields was 3C286 and the phase calibrators were 1727+455 for the Hercules and 0832+492 for the Lynx field.

The data were again calibrated using the NRAO AIPS package. Each calibrated source observation was edited to remove bad data and then CLEANed using 10000 iterations, with a pixel size of $0.15''$ and nearly pure uniform weighting to avoid downweighting the longest, PieTown, baselines and thus achieve high resolution images. The noise level reached for each source observation is given in Table 3 above and the resolution of the images was typically $1.1'' \times 0.6''$ with the highest resolution direction determined by the location of the PieTown antenna.

All the candidate sources included in the VLA+Pt observations were detected and their flux densities were then measured with *tvstat*; these can be found in Table 3. The corresponding contour plots can be found in Figures B1 and B2.

3.2 MERLIN observations

The MERLIN observations were done in wide-field mode, with an individual field size of about $2.5'$ radius; at this distance from the pointing centre the bandwidth smearing is $< 10\%$. Three of these

Table 3. Details of the VLA+Pt exposure times for the Lynx and Hercules high-redshift candidate sources, along with the resulting flux densities and noise limits.

Hercules			
Source Name	Exposure Time (s)	$S_{1.4\text{GHz}}$ (mJy)	rms (μJy)
53w054a	2600	1.82 ± 0.07	29
53w054b	2600	2.58 ± 0.07	29
53w059	2580	21.23 ± 0.21	30
53w061	2580	1.68 ± 0.06	28
53w065	2590	6.26 ± 0.09	33
53w069	2570	3.50 ± 0.18	36
53w087	2600	4.19 ± 0.17	28
53w088	2590	14.11 ± 0.09	30
Lynx			
55w116	2550	0.91 ± 0.16	49
55w120	2570	0.98 ± 0.13	47
55w121	2560	1.32 ± 0.11	43
55w128	2570	2.94 ± 0.45	47
55w132	2560	1.02 ± 0.19	45
55w133	2570	2.23 ± 0.14	44
55w136	2580	0.76 ± 0.17	44
55w138	2570	1.74 ± 0.18	45

sub-fields were used in the Hercules field and 4 in the Lynx field. The pointing positions were designed such that the maximum number of non-candidate sources could also be observed whilst still including as many of the candidates as possible. Whilst these extra sources were not selected as high-redshift FRI candidates, observing them at higher-resolution may help to classify some of the lower redshift objects in the sample. 53w091, one of the sources not included in the complete sample, was also included in the MERLIN observations as a result of this process.

MERLIN consists of up to seven antennas spread across the UK, giving baselines up to 217 km and a resolution, at L-band, of $\sim 0.15''$. The sources were observed with MERLIN on 11th March 2005 for the Hercules and on 13th, 19th, 20th, 28th and 29th May 2006 for the Lynx field, both using 32 channels, with a combined bandwidth of 15.5 MHz. It should be noted that due to technical problems the Lovell telescope, the largest antenna in the array, was only included in the observations of Lynx B, C and D; this increased the sensitivity for these sub-fields by a factor of ~ 2.2 .

For the Hercules subfields, the flux calibrators used were 3C286 and OQ208 and the phase calibrator was 1734+508. For three of the Lynx subfields (B, C and D), the flux calibrators were again 3C286 and OQ208; for Lynx A, however, 3C286 and 2134+004 were used. The Lynx phase calibrator was 0843+463. Two flux calibrators are necessary as 3C286 is resolved on all but the shortest MERLIN baselines. All subfields were observed for 12 hours.

The initial editing and calibration of the data was done at Jodrell Bank using local software specially written for the MERLIN array. Following this the data were loaded into AIPS and the MERLIN pipeline (Diamond et al. 2003), which uses the AIPS calibration tasks with MERLIN specific inputs, was then used to complete the calibration. Data which included the Lovell telescope were then reweighted to account for the different sensitivities of the instruments in the array.

Finally each subfield was Fourier transformed and deconvolved to form the final CLEANed image. To minimise the non-

Table 4. The primary beam corrected flux densities and un-primary beam corrected noise levels found from the Hercules MERLIN observations. A * indicates a source which was resolved out. All flux densities were measured using *tvstat*. A primary beam correction error of 20% of the difference between the corrected and un-corrected flux density has been incorporated into the quoted errors.

Hercules				
Sub-field	Name	$S_{1.4\text{GHz}}$ (mJy)	C_{PB}	rms (μJy)
A	53w054a	1.47 ± 0.13	1.03	41
A	53w054b	1.83 ± 0.13	1.02	41
A	53w057	2.04 ± 0.14	1.00	40
B	53w059	18.87 ± 0.62	1.06	46
A	53w061	1.06 ± 0.10	1.03	34
B	53w065	4.62 ± 0.18	1.05	46
B	53w066	3.32 ± 0.18	1.00	47
B	53w070	2.29 ± 0.15	1.08	46
C	53w087	*		43
C	53w088	10.80 ± 0.18	1.05	49
Extra sources				
C	53w082	2.40 ± 0.15	1.09	45
C	53w089	*		42
C	53w091	32.81 ± 1.00	1.04	47

coplanar array effects the centre of each subfield was again shifted to the position of each source it contained and treated separately. Each source facet was 512 by 512 pixels with $0.045''/\text{pixel}$. The rms noise reached for each source was between 27 and 49 μJy , and can be found in Tables 4 and 5. This process was then repeated for Lynx subfields B, C and D, with all baselines including the Lovell telescope removed from the data. This was done as, without Lovell, a 76 m diameter dish, the MERLIN antennae are all comparable in size (similar to those of the VLA) and so a simple primary beam correction method can be applied. The non-Lovell images were therefore used to measure the primary-beam corrected flux densities of the sources but the deeper, Lovell included, images were used for the morphological classification. The rms noise reached in the non-Lovell images can also be found in Table 5.

For the Hercules sources, one candidate and one of the ‘extra’ sources were resolved out; the rest were all detected. In the Lynx subfields all the candidates were detected and 3 of the ‘extra’ sources were resolved out. A primary beam correction was then applied to correct for the attenuation of the primary beam on the off-centre sources and the flux densities were measured; the resulting values can be found in Tables 4 and 5. The corresponding contour maps can be found in Figures B1 and B2.

3.3 Comparison of results

Comparing the flux density values at the different radio resolutions, it is clear that, for many of the sources, the measured flux density decreases as the resolution of the observations increases. For the non-quasar sources, it is likely that this loss indicates the presence of resolved-out, extended emission, which in the absence of hotspots may indicate an FRI-type structure. The four quasars in the sample are variable at some level, so any flux density loss they exhibit may be due to this.

Since the resolutions of the four radio observations are so different, it is hard to gain an overview of the structure of individual sources in the sample from considering the respective contour maps

Table 5. The primary beam corrected flux densities and un-primary beam corrected noise levels, both with and without the Lovell telescope in the array, found from the Lynx MERLIN observations. A * indicates a source which was resolved out. A primary beam correction error of 20% of the difference between the corrected and un-corrected flux density has been incorporated into the quoted errors. A ‘T’ indicates a *tvstat* measurement and an ‘I’ indicates an *imfit* measurement.

Lynx							
Sub-field	Name	$S_{1.4\text{GHz}}$ (mJy)	C_{PB}	Measure	rms (Lovell) (μJy)	rms (no Lovell) (μJy)	
C	55w116	1.68 ± 0.34	1.06	T	30	68	
C	55w121	0.97 ± 0.14	1.05	I	32	71	
B	55w128	1.52 ± 0.32	1.04	T	29	67	
B	55w132	1.29 ± 0.31	1.01	T	28	65	
D	55w133	1.63 ± 0.17	1.04	I	30	68	
D	55w136	0.44 ± 0.19	1.04	T	28	68	
B	55w138	1.16 ± 0.26	1.01	T	30	67	
D	55w143a	1.73 ± 0.20	1.05	T	37	62	
A	55w159a	4.71 ± 0.18	1.04	I	—	98	
Extra sources							
C	55w118	0.77 ± 0.19	1.01	I	32	68	
C	55w122	0.32 ± 0.15	1.07	I	30	67	
C	55w123	1.01 ± 0.12	1.03	I	33	70	
C	55w124	3.26 ± 0.14	1.05	I	32	76	
B	55w127	1.31 ± 0.31	1.08	T	27	64	
B	55w131	*			28	65	
B	55w137	1.14 ± 0.17	1.02	T	28	63	
D	55w141	0.26 ± 0.10	1.02	I	32	66	
D	55w143b	0.31 ± 0.11	1.04	I	33	67	
A	55w150	*			—	102	
A	55w157	2.51 ± 0.30	1.04	I	—	108	
A	55w159b	*	1.04		—	96	
C	60w016	0.48 ± 0.16	1.02	T	33	72	

separately. Therefore, Figures B1 and B2 show, for the sources included in the VLA+Pt or MERLIN observations, all the available radio contour maps at the same scale, centred on the optical host galaxy positions, if available, or otherwise on the A–array position¹. Collecting the images together like this illustrates the power of the high resolution observations in differentiating FRI objects from FRIIs. For example, the Hercules field source 53w059 is an FRI candidate in the A–array data but it is only in the MERLIN map, showing its inner jet and resolved out lobes, that it can be firmly classified as such. On the other hand, the A–array image of the Lynx field source 55w138 does not show any clear structure and whilst the VLA+Pt map indicates that it is extended, the MERLIN map is needed to show the location of the jet hotspots.

4 FRI IDENTIFICATION AND CLASSIFICATION

The most secure method of FRI classification, the detection of weak extended emission relative to a compact core, is impossible for the majority of the sample sources due to the lack of firm jet detections. FRI-type, as described above, can also be inferred by comparing the source flux densities at the low and high resolutions; a drop in flux density indicates the presence of resolved-out, extended emission, which in the absence of hotspots is likely to be due to an FRI.

The classifications were therefore done by inspecting the source morphologies where possible, or by using the flux-loss

method where not, ignoring the possibly variable quasars. However, since the comparison between the Oort et al. (1987; 1985) and the A–array data cannot be relied upon to determine flux density loss, as discussed in Paper I, the only loss comparison that could be done for the Hercules field was between the A–array and VLA+Pt or MERLIN data. As a result, Hercules sources which were not covered by the higher-resolution observations, and which showed no obvious FRI-type jets in the A–array radio maps, could not be firmly classified. For the Lynx field sources, the existence of the B–array observations, which are of a similar resolution to the Oort et al. (1985) data, meant that these could be used for a more internally consistent comparison with the A–array, MERLIN and VLA+Pt data, instead.

Considering all these factors, five classification groups were defined for the sample. Group:

- (i) = Certain FRIs – these clearly show typical weak, edge-darkened, FRI jets and compact cores,
- (ii) = Likely FRIs – these show some morphological extension consistent with an FRI structure, but not enough to be definitely classified as FRIs, along with a flux loss of 3σ or greater at higher resolution,
- (iii) = Possible FRIs – either no extension is seen for these sources but they still lose $\geq 3\sigma$ of their flux when going to higher resolution, or some extension consistent with an FRI structure is seen but little flux is lost,
- (iv) = Not FRIs – this group consists of sources which either have no flux loss or have FRII-type morphology,
- (v) = Unclassifiable sources – this group is for sources in the

¹ The starburst galaxy 55w127 is not included in this Figure as it is not an FRI candidate

Hercules field which are compact in the A–array maps, lose no flux between the Oort et al. and A–array data and were not included in the higher resolution observations.

The flux density loss between all the different observations was calculated using $(1 - \frac{S_{\text{hr}}}{S_{\text{lr}}})$, where S_{hr} and S_{lr} are the flux densities measured in the higher and lower resolutions respectively. The σ values for these losses were then found by dividing the loss by its corresponding error; these can be found in Tables 6 and 7 with $>3\sigma$ losses highlighted in bold. Each source was classified into one of the groups in turn using the flowchart shown in Figure 1. For the sources that were classified by morphology alone, the process was repeated by all three authors independently to ensure that the results were consistent. If there was a disagreement between the three testers, the median grouping value was taken. The results given by each tester, along with the final groups assigned to these, and the rest of the sample, can be found in Tables 6 and 7. Additionally, the two FRIs detected in the Hubble Deep and Flanking fields (Snellen & Best 2001) were incorporated into the sample, and the HDF+HFF area ($10 \times 10 \text{ arcmin}^2$) was added in to the Hercules and Lynx areas determined by the optical imaging. Both of these FRIs are added to group 1; since the entire HDF+HFF area has been covered by very deep high resolution (0.2 arcsec) radio imaging (Muxlow et al. 2005), all sources are definitively classified and there are no group 2 or 3 sources. The two FRI sources detected here is slightly higher than the ~ 1 FRI predicted for this sky area from the maximal surface density in the Lynx and Hercules fields, but is within the errors: including this region does not significantly change our results but does improve the statistics.

5 INVESTIGATING THE FRI SUBSAMPLE

Now that the radio sample has been classified, the sources in groups 1–3 (the certain, likely and possible FRIs) can be used to investigate the changes in co-moving space density out to high redshift. To ensure that this measurement is robust out to a significant distance, a 1.4 GHz radio power limit (P_{lim}) of $\geq 10^{25} \text{ W/Hz}$, was imposed on the sample. This limit corresponds to a maximum redshift, z_{max} , of 1.86 out to which a source at the 0.5 mJy sample flux density limit, and with a typical spectral index, α , of 0.8, could be seen.

There is a possibility that group 5, the ‘Unclassifiable sources’, contains FRIs which should be included in the space density analysis. However, of the 6 sources which fall into this category, half are at $z \sim 0.6$ and half lie at $z > z_{\text{max}}$. Since it is the $z \sim 1.0$ redshift behaviour that is being investigated here, these missing sources should not significantly affect the results.

This section describes the steps taken to measure the minimal and maximal co-moving space density of the three FRI groups in the sample. Firstly, the parameters and techniques used for the measurement are defined, followed by the methods used to determine the local FRI space density, and finally, the results of the space-density calculation are presented.

5.1 The evolving FRI space density

The space densities were calculated using the $1/V_{\text{max}}$ statistic, where the space density, ρ , of N sources in some redshift bin Δz is simply

$$\rho_{\Delta z} = \sum_{i=0}^N \frac{w_i}{V_i} \quad (1)$$

Table 6. The σ flux density loss and classification groups (for the three testers in no particular order) for the sources in the Hercules field complete sample with values of $>3\sigma$ highlighted in bold. A, P and M represent the VLA A–array, VLA A+Pt and MERLIN observations respectively. A ‘*’ indicates a source which was resolved out in the MERLIN observations. Sources previously classified as starburst galaxies and quasars are labelled with the superscripts ‘SB’ and ‘Q’ respectively.

Name	$\sigma_{\text{P/A}}$	$\sigma_{\text{M/A}}$	Test 1	Test 2	Test 3	Final
			Group	Group	Group	Group
53w052						3
53w054a	1.06	2.46				4
53w054b	-0.40	2.22				4
53w057		-0.35				4
53w059	2.35	4.33	1	1	1	1
53w061 ^Q	-1.07	2.22				3
53w062						5
53w065	-2.16	5.96				2
53w066		5.81	3	3	2	3
53w067			1	2	1	1
53w069		6.33	2	1	1	1
53w070		1.54				4
53w075 ^Q						4
53w076			2	2	1	2
53w077		4	4	4	4	4
53w078						3
53w079						5
53w080 ^Q			4	4	4	4
53w081						5
53w082		1.38				4
53w083						5
53w084						5
53w085						3
53w086a			2	3	2	2
53w086b			3	3	2	3
53w087	15.08	*				2
53w088	0.14	1.71				3
53w089		*				3
66w009a						4
66w009b ^{SB}						4
66w014						4
66w027 ^{SB}						4
66w031						3
66w035			3	3	2	3
66w036			2	3	1	2
66w042			2	2	1	2
66w047						3
66w049						4
66w058						5

where V_i is the volume over which a source i , with weight w_i , could be seen in a particular bin. Four redshift bins of width 0.5, covering the range $0.0 < z \leq 2.0$ were used for the sample. The upper end of the final, $z = 1.5 - 2.0$, bin exceeded the value of z_{max} corresponding to the limiting flux density for $\alpha = 0.8$; as a result the individual maximum redshifts of the sources in this bin were determined, so that only the volumes over which each source could be observed were used to find the density here.

It should be noted that the redshift limit strongly depends on the value of α used; as the spectral index steepens from 0.5 to 1.5, z_{max} decreases from 2.16 to 1.43. It is important to stress that α needs to be ≥ 1.37 before z_{max} falls below the start of the final redshift bin, for the limiting power of 10^{25} W/Hz . This spectral index is steeper than that found for essentially all radio sources

Table 7. The σ flux density loss and classification group (for the three testers in no particular order) for the sources in the Lynx field complete sample with values of $>3\sigma$ highlighted in bold. B, A, P and M represent the VLA A and B-array, VLA A+Pt and MERLIN observations respectively. A ‘**’ indicates a source which was resolved out in the MERLIN observations. Sources previously classified as starburst galaxies and quasars are labelled with the superscripts ‘SB’ and ‘Q’ respectively.

Name	$\sigma_{A/B}$	$\sigma_{P/B}$	$\sigma_{P/A}$	$\sigma_{M/B}$	$\sigma_{M/A}$	Test 1	Test 2	Test 3	Final Group
						Group			
55w116	1.30	4.59	2.79	0.75	-0.36	4	3	3	3
55w118	0.68			0.36	-0.13				4
55w120	0.50	3.64	3.26			2	3	2	2
55w121	1.23	-0.43	-1.54	1.52	0.40				3
55w122	0.51			2.62	2.12				3
55w123	-0.47			0.45	1.14				4
55w124 ^Q	-1.10			-3.55	-2.01				4
55w127 ^{SB}	0.52			1.26	1.01				4
55w128	-0.79	1.92	3.26	6.71	8.86	1	2	1	1
55w131	2.77			*	*	2	2	1	2
55w132	0.43	2.98	2.74	1.36	1.04	4	3	3	3
55w133	-0.38	-0.31	0.09	2.75	3.01				2
55w135 ^{SB}	-1.80								4
55w136	-0.15	0.72	0.87	2.38	2.54	4	4	3	4
55w137	0.20				2.69	2.74			3
55w138	-0.91	0.33	1.13	2.78	3.08	3	4	2	3
55w140 ^Q	0.29								4
55w141	1.70			3.07	1.59				3
55w143a	0.18			2.28	2.08	3	3	2	3
55w143b	3.01			2.49	0.16				3
55w147	1.19								4
55w149	-0.12					1	1	1	1
55w150	-0.17								4
55w154	-1.31					1	1	1	1
55w155	-0.33								4
55w156	-2.01					1	1	1	1
55w157	2.34			-2.48	-3.26				4
55w159a	0.14			4.17	2.42	2	2	2	2
55w159b	0.23			*	*				3
55w160	-0.34								4
55w161	-1.39								3
55w165a	-0.65					1	1	1	1
55w165b	2.36								4
55w166	-0.16								4
60w016	-1.14			0.45	2.28				3
60w024	-0.93								4
60w032	-0.97								4
60w039 ^{SB}	-0.35								4
60w055	-0.05								4
60w067	0.74								4
60w071	0.38								4
60w084	-1.75								3

which suggests that the space density results in the $z < 1.5$ bins are robust to changes in the assumed value of α . Therefore, it is only in the final, $1.5 < z < 2.0$, bin that the values of V_i (and hence the density) depend on the assumed value of α ; the V_i s for sources in the other bins are all the full bin volume. In reality though, the 3 sources that do lie in the last bin have flux densities which are all much greater than the 0.5 mJy limit (the faintest is 4.53 mJy), and consequently the result does not change if α is varied.

The three different FRI classification groups used meant that a minimum (8 sources; group 1 only), maximum (16 sources; groups 1, 2 and 3) and probable (12 sources; groups 1 and 2) FRI space density could be calculated. The flux densities used to calculate the source radio powers are those resulting from the A–array observations (Paper I), and sources that were previously classified as

starburst galaxies have been removed from the sample. The average luminosity in each bin can be found in Table 8; they indicate that there is a small luminosity–redshift trend but the effect of this has been largely mitigated by the P_{lim} limit. The spectral indices for 51% of the Hercules field sources were taken from Waddington et al. (2000); for the remainder of the sample α was assumed to be 0.8. The validity of this assumption was tested by recalculating the radio powers using two extreme α values of 0.5 and 1.8 for all the sources in the sample. Up to and including these limits, the number of sources in each bin does not change.

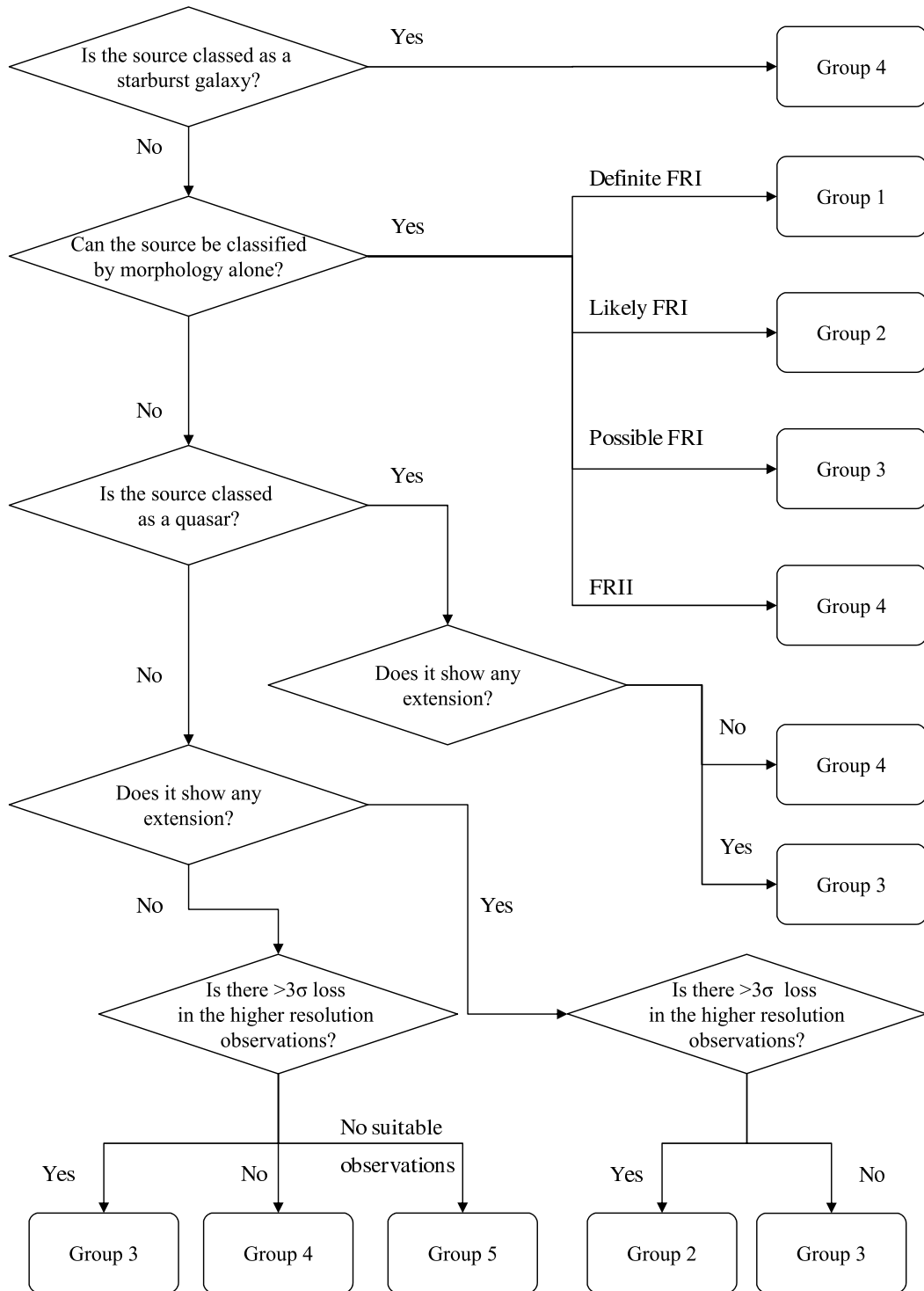


Figure 1. The procedure followed for the source morphological classification.

5.2 The local FRI space density

An accurate measurement of the local FRI space density is vital for determining whether the sample described here demonstrates a density enhancement at high redshift. This can be obtained by di-

rectly measuring the FRI numbers in two different local, complete, radio samples.

The first local measurement was carried out using a complete subsample of the 3CR galaxy survey (Laing, Riley & Longair 1983) which contains 30 FRI sources with $S_{178\text{MHz}} \geq 10.9$ Jy

(corresponding to $S_{1.4\text{GHz}} \geq 2.09$ Jy, using $\alpha = 0.8$), in an area of 4.24 sr. A source with power $P_{\text{lim}} = 10^{25}$ W/Hz and $\alpha = 0.8$, can be seen out to a redshift of 0.046 if it was in this survey. Converting the 3CR flux densities to 1.4 GHz using their published spectral indices (Laing, Riley & Longair 1983), it was found that there were 4 FRIs with $P_{1.4\text{GHz}} \geq P_{\text{lim}}$ in the comoving volume of $V(z \leq 0.046) \times (4.24/4\pi) = 1.0 \times 10^7 \text{ Mpc}^3$, which gives a local space density of $402 \pm 201 \text{ FRIs/Gpc}^3$.

The second local sample used was the equatorial radio galaxy survey of Best et al. (1999) which contains 178 sources, including 9 FRIs, with $S_{408\text{MHz}} > 5$ Jy (corresponding to $S_{1.4\text{GHz}} > 1.9$ Jy, again using $\alpha = 0.8$), in an area of 3.66 sr. In this survey a source at P_{lim} can be seen out to $z = 0.048$; there are 2 FRIs in this volume with powers greater or equal to this which gives a local density of $196 \pm 139 \text{ FRIs/Gpc}^3$.

Combining the results from these two surveys gives a total of 6 FRI sources in a comoving volume of $2.0 \times 10^7 \text{ Mpc}^3$ and a corresponding comoving local FRI space density of $298 \pm 122 \text{ FRIs/Gpc}^3$.

An alternative estimate can be obtained by integrating the local radio luminosity function of Best et al. (2005), which was calculated from a sample of 2215 radio-loud AGN, formed by comparing the SDSS with two radio surveys: the National Radio Astronomy Observatories (NRAO) Very Large Array (VLA) Sky Survey (NVSS) (Condon et al. 1998) and the Faint Images of the Radio Sky at Twenty centimetres (FIRST) survey (Becker, White & Helfand 1995).

Since the radio luminosity function decreases rapidly above $\log P = 24.5$, the calculated total number is not strongly dependent on the chosen value for the upper limit of the integration. Although there will be some FRIIs included, the majority of sources will be FRIs, therefore integrating out to ∞ will derive a maximal FRI space density which ought also to be close to the true value. This calculation gives 460 FRIs/Gpc³ brighter than 10^{25} W/Hz, which is in good agreement with the values calculated by the two direct measurements.

5.3 Results of the space density calculation

Figure 2 shows the results of the space density calculation (calculated using Equation 1) for the 4 redshift bins, plotted at the bin midpoints; the numbers are given in Table 8 and the weights used for each source can be found in Paper I.

The space densities for the minimum, probable and maximum FRI groups show a high redshift comoving density enhancement for the FRIs in this sample, compared to the local FRI space density. The turnover in space density seen at $z \gtrsim 1.5$ is supported by the work of Waddington et al. (2001) who found evidence for a high redshift cut-off for their lower luminosity radio sources by $z \simeq 1 - 1.5$. However, since the values of V_i in the last bin can depend on assumed spectral indices, the addition of a small number of steep spectrum sources, close to the luminosity limit, would result in a large increase in density; for example, ~ 3 more sources of flux density S_{lim} and $\alpha = 1.0$ would be needed to give the same maximum value of ρ as in the previous $1.0 < z < 1.5$ bin. Sources may also have been missed in this bin because of the strong observational bias against FRIs at these distances (i.e. a clear Group 1 source at $z = 1$ could be classified as a Group 3 source if it was at $z = 2$).

Two potential concerns in calculating the space densities are

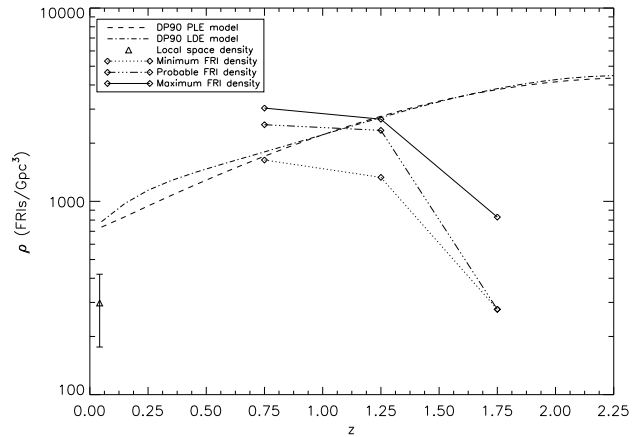


Figure 2. The space density changes in redshift bins of width 0.5, plotted at the bin midpoints. Also shown are the PLE and LDE models of DP90, converted to 1.4 GHz and to this cosmology, for comparison; see §5.3.1 for a full description of these models. Since no sources with $P > 10^{25}$ W/Hz were found in the first redshift bin, no space density value is plotted there.

the estimated redshifts² and the assumed spectral indices of 0.8 used for some of the sample sources. Error in both of these factors could affect the radio power determination, and lead to sources falsely falling below P_{lim} , whilst error in the former alone could also move sources between redshift bins. To investigate the effect of these on the results, two Monte Carlo simulations, with 10,000 iterations each, were performed. In the first simulation, in each iteration, the redshifts which were estimated were varied by a factor drawn randomly from a Gaussian distribution of width equal to 0.2 in $\log z$, the approximate spread in both the $r-z$ and $K-z$ relations. Similarly, in the second simulation, in each iteration, the assumed spectral indices were varied from 0.8 by a factor drawn randomly from a Gaussian distribution of width 0.5. This value was chosen as it represents a reasonable spread in α . Figure 3 shows the $\pm 1\sigma$ density results of the two simulations, carried out for the probable FRIs (i.e. groups 1 and 2) only. Also shown are the errors on the densities calculated from the simple Poisson errors on the number of sources in each bin (for the bin containing no sources, an error of ± 1 source was assumed). These results are also given in numerical form in Table 9. It is clear from this that the major limiting factor for the results is the small number of sources in the sample, rather than the redshift estimates, or the assumed spectral indices, that were used for some of the sources. It should also be noted that the radio FRI classifications are as comparably large a source of error as the redshift estimates.

5.3.1 Quantifying the space density enhancement

The calculations above show that the uncertainty in the space density results is dominated by the Poissonian error. In order to better quantify the high redshift enhancements therefore, the density calculation was repeated using a single, large, redshift bin spanning $0.5 < z < 1.5$, containing a minimum of 7 and a maximum of 13 FRI sources. The resulting densities can also be found in Table

² A full description of the redshift estimation methods used, and the results obtained for those sample sources without a secure redshift, can be found in Paper I

Table 8. The results of the space density calculations for both redshift bin sizes, for the limiting power of 10^{25} W/Hz. ‘No.’ is the number of sources in each bin and \bar{P} is the mean luminosity in each bin. Also shown are the results of the space density calculations using the additional luminosity limits $P \geq 10^{24}$ and $P \geq 10^{24.5}$ W/Hz. All results are shown for the maximum, minimum and probable FRI numbers.

Bin	No.	Minimum		Probable		Maximum	
		$\log \bar{P}$	ρ (FRIs/Gpc 3)	$\log \bar{P}$	ρ (FRIs/Gpc 3)	$\log \bar{P}$	ρ (FRIs/Gpc 3)
$P \geq 10^{25.0}$ W/Hz							
0.0 < $z \leq 0.5$	0	–	0	0	–	0	0
0.5 < $z \leq 1.0$	3	25.7	1636	4	25.6	2492	5
1.0 < $z \leq 1.5$	4	25.6	1331	7	25.6	2329	8
1.5 < $z \leq 2.0$	1	26.6	276	1	26.6	276	3
0.5 < $z \leq 1.5$	7	25.6	1446	11	25.6	2391	13
$P \geq 10^{24.5}$ W/Hz							
0.0 < $z \leq 0.5$	1	24.7	2442	2	24.6	4884	3
0.5 < $z \leq 1.0$	3	25.7	1636	5	25.5	3370	8
1.0 < $z \leq 1.5$	4	25.6	1331	8	25.6	2882	9
$P \geq 10^{24.0}$ W/Hz							
0.0 < $z \leq 0.5$	1	24.7	2442	3	24.6	7546	4
0.5 < $z \leq 1.0$	3	25.7	1636	5	25.5	3370	10

Table 9. The errors calculated from the Monte Carlo simulations, $z \sigma_{mc}$ and $\alpha \sigma_{mc}$, along with the Poissonian, σ_p , errors and the spread in the calculated space densities for each redshift bin ($\rho_{\max} - \rho_{\min}$); all values are in FRIs/Gpc 3 . Also shown is the probable FRI space density, ρ_{prob} .

	0.0 < $z \leq 0.5$	0.5 < $z \leq 1.0$	1.0 < $z \leq 1.5$	1.5 < $z \leq 2.0$
ρ_{prob}	0	2492	2329	276
$\rho_{\max} - \rho_{\min}$	0	1401	1331	553
$z \sigma_{mc}$	810	496	391	257
$\alpha \sigma_{mc}$	0	345	124	0
σ_p	2442	1246	880	276

8; they show enhancements of 3.2σ , 2.9σ and 2.1σ over the local FRI space density, for the maximum, probable and minimum groupings respectively.

Measuring these significance levels is not the best way of judging the reliability of the space density increase, however. A better method, following Snellen & Best (2001), is to assume no evolution of the FRI population and then calculate the probability of detecting the numbers of minimum ($P_{>7}$), probable ($P_{>11}$) and maximum ($P_{>13}$) objects seen in the $0.5 < z < 1.5$ bin, if this no-evolution scenario was correct. The volume contained within this bin is 0.005 Gpc 3 which, assuming no evolution occurs from a local density of 298 FRIs/Gpc 3 , gives an expected number of 1.44 FRIs over this range. (For comparison, repeating this calculation for $z < 0.5$ suggests that 0.12 FRIs should have been detected in the sample, in this volume, for a constant co-moving space density.) The resulting probabilities are summarized in Table 10. These are all $\ll 1\%$ which indicates that, as expected, the no-evolutionary scenario can be discounted.

The pure luminosity evolution (PLE) and luminosity/density evolution (LDE) models of DP90, which fit the overall radio source population well out to $z \sim 2$, can also be compared to the results using this method. If the behaviour of the FRIs here is consistent with these PLE and LDE models, this would suggest that they evolve in the same way as FRII objects of the same radio power.

Table 10. The probabilities calculated for the no-evolution, PLE and LDE scenarios for the minimum, probable and maximum numbers of FRIs.

	Expected Number	$P_{>7}$	$P_{>11}$	$P_{>13}$
No Evolution	1.44	0.07%	$3.8 \times 10^{-5}\%$	$4.9 \times 10^{-7}\%$
PLE	11.63	94%	61%	38%
LDE	11.67	95%	62%	39%

In the PLE model, the local radio luminosity function (fitted using a dual power-law, with a steeper slope, for the higher powered sources, above the luminosity break) shifts horizontally in the $\rho-z$ plane only, and its overall shape does not change. These redshift changes were confined to the luminosity normalization, P_c , only and DP90 parameterized these as a quadratic in $\log z$. Conversely, in the LDE model, the local RLF can move both horizontally and vertically and, therefore, can steepen or flatten. As a result, DP90 allowed the density normalization, ρ_0 , to also vary with redshift. For full details of these two models, the reader is referred to Section 3.4 of DP90.

For each of these two models, the total number of sources in

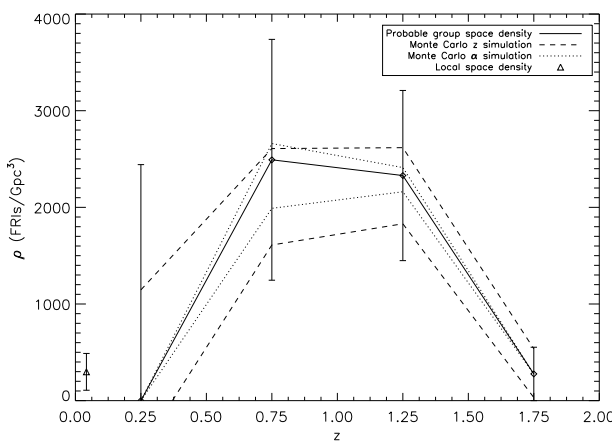


Figure 3. The space density changes and Poisson errors of the probable group of objects, with $P \geq 10^{25}$ W/Hz, overplotted with the $\pm 1\sigma$ results of the redshift and spectral index Monte Carlo simulations. Both sets of results clearly show that it is the small number of sources in each bin that has the most effect on the results.

the interval $0.5 < z < 1.5$ was found by integrating

$$N_{\text{tot}} = \Omega \int_{0.5}^{1.5} \int_{P1}^{P2} \rho(P, z) dV(z) \quad (2)$$

where Ω is the area of the survey in steradians and the luminosity limits of the integration are $P1 = 10^{25}$ W/Hz and $P2 = 10^{27.5}$ W/Hz. The co-efficients used in these calculations were those determined for the steep spectrum population by DP90. Where necessary these values were converted from their original 2.7 GHz to 1.4 GHz, the frequency used here, again assuming an average α of 0.8. Changing this assumption does not significantly alter the final results. Additionally, since the DP90 models were determined using Einstein de Sitter (EdeS) cosmology, the luminosity limits actually used for the integration were the EdeS values corresponding to $P1$ and $P2$ at each redshift step to ensure that the correct, concordance cosmology, values of N_{tot} were found.

Carrying out the integrations results in $N_{\text{tot}} \sim 11$ for both models, over this redshift range, and corresponding enhancements over the local value used here of ~ 8 . This expected number agrees very well with the observed numbers of 7, 11 and 13 for the minimum, probable and maximum samples, confirming that these space densities can be consistent with these models. The subsequent probabilities arising from these numbers can again be found in Table 10. This result is further supported by Figure 2, in which the density values predicted by the PLE and LDE models are overplotted with the results previously calculated for the 4 redshift bins. The low redshift disagreement seen between the models and the local FRI space density is likely to arise from the poor constraints locally, at these radio powers, in the DP90 results.

5.3.2 Including the lower luminosity FRIs

The space density calculation can be repeated using different luminosity limits to investigate the behaviour of the weaker sources in the sample. Figures 4 and 5 show the results of this for limits of 10^{24} and $10^{24.5}$ W/Hz and the density values are given in Table 8. The calculation was, in both cases, carried out for the minimum, maximum and probable numbers of FRI, using redshift bins

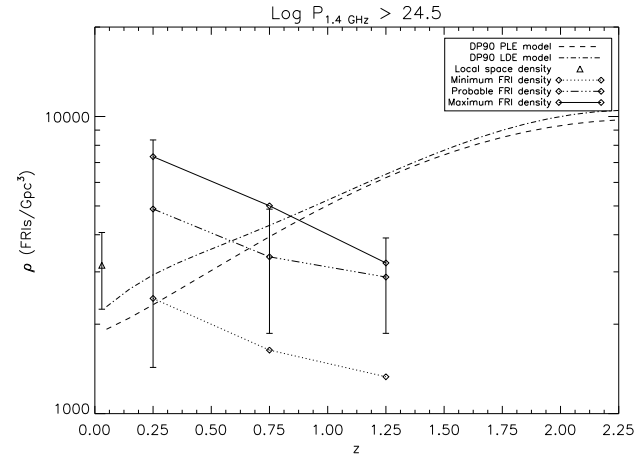


Figure 4. The space density changes in redshift bins of width 0.5, plotted at the bin midpoints for $P > 10^{24.5}$ W/Hz. For comparison the redshift axis is plotted with the same range as in Figure 2 and the PLE and LDE models of DP90 are again shown, along with Poisson errors for the probable group of objects.

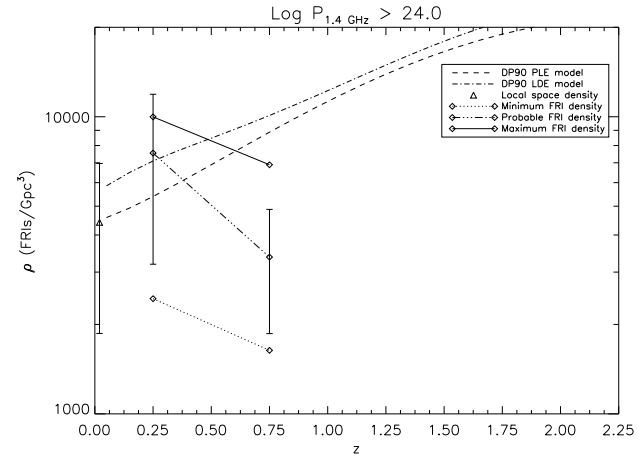


Figure 5. The space density changes in redshift bins of width 0.5, plotted at the bin midpoints for $P > 10^{24}$ W/Hz. For comparison the redshift axis is plotted with the same range as in Figure 2 and the PLE and LDE models of DP90 are again shown, along with Poisson errors for the probable group of objects.

of width 0.5, with the final bin dependent on the value of the limiting luminosity as discussed previously. The local values were again found using a combination of the 3CR and equatorial galaxy samples.

The comoving space densities for these two new limits indicate that the enhancement over the local values in both cases is smaller than that seen when $P_{\text{lim}} = 10^{25}$ W/Hz (Figure 2). These results are supported by the work of Sadler et al. (2007) who found that the cosmic evolution of their low power ($10^{24} \leq P_{1.4\text{GHz}} < 10^{25}$ W/Hz) population was significant but less rapid than that seen for their higher powered sources.

Inspection of Figures 4 and 5 also suggests that the peak comoving density moves to lower redshifts at lower luminosities, though the large errors on these results, and the restricted redshift range sampled at these low powers prohibit strong conclusions from being drawn.

6 SUMMARY AND DISCUSSION

The radio observations presented here, along with the data previously presented in Paper I, allowed the 81 sources of the complete sample to be classified into 5 groups: Group 1 was for secure, morphologically classified, FRIs; Group 2 for sources with indications of FRI-type extension, alongside a flux density loss of 3σ or more; Group 3 for sources with either flux density loss or some extension, and Groups 4 and 5 for sources which were either definitely not FRIs or which were unclassifiable. The FRIs in the sample, together with the two FRIs in the Hubble Deep and Flanking Fields, were then used to calculate the maximum, probable and minimum space densities over the range $0.0 < z < 2.0$. The main results of this calculation are listed below.

- (i) Clear density enhancements, by a factor 5–9, were seen at $z \sim 1.0$, over the local FRI value, for FRIs brighter than 10^{25} W/Hz,
- (ii) This result is secure, with the main source of error arising from the low number of sources in the FRI subsample,
- (iii) The no-evolution scenario was ruled out at the $>99.9\%$ confidence limit,
- (iv) The results were consistent with previously published models which in turn suggests that, at a particular radio power, FRIs evolve like FRIIs.
- (v) The results also indicate that the FRI evolution may be luminosity dependent, with lower powered sources evolving less strongly, and the peak in space density possibly moving to lower redshifts for weaker objects.

Now that the space density enhancements of this sample have been determined it is useful to compare them to the results of previous work. Sadler et al. (2007), for instance, found increases in space density, out to $z = 0.7$, by a factor of $\sim 2 - 10$ for the high ($P_{1.4\text{GHz}} > 10^{25}$ W/Hz) luminosity radio galaxies in their sample; these are consistent with the range of enhancements ($\sim 5 - \sim 9$) to $z \sim 1$ seen in the large redshift bin here. Jamrozy et al. (2004) also find that positive evolution, this time PLE, of the form $\rho(z) = \rho(0) \exp(M(L)\tau)$ (where $\tau = 1 - (1+z)^{-1.5}$ and the evolution rate, $M(L)$, was found to be 5.0), is necessary to fit the number counts of the highest luminosity, morphologically selected, FRIs in their sample. At $z = 1$ this corresponds to an enhancement of 25 which is significantly higher than that seen here. Additionally, Willott et al. (2001) see a rise of about one dex, between $z \sim 0$ and $z \sim 1$, in the comoving space density of their low luminosity, weak emission line, population which contains mainly FRI sources, along with some FRIIs. It should be noted that other studies of radio galaxy evolution do not directly measure the amount of space density evolution present in their samples. Instead they test for evolution using the V/V_{max} statistic and therefore cannot be directly compared to the results of this work.

In general, all the previous studies of radio galaxy evolution conclude that the more luminous sources undergo more cosmic evolution. For samples in which the FRI population was determined by a luminosity cut, this tends to imply little or no evolution for these sources (e.g. the lower luminosity sources of Clewley & Jarvis (2004) show no evolution, whereas evolution is seen for sources of comparable luminosity to those here). However, for samples which either morphologically classify their sources or which apply a different dual-population scheme (e.g. the low/high luminosity division based on line luminosity of Willott et al. (2001)), evolution of at least some of the FRIs objects is typically seen. It would seem, therefore, that the previous models in which all FRIs

have constant space density, whereas all FRIIs undergo strong, positive, cosmic evolution, are too simplistic and do not accurately represent the behaviour of the FRI-type objects. A better representation of the FRI/II space density evolution seen here and in other work, is the picture in which as the luminosity of a source increases, so does the amount of positive evolution it undergoes between $z \sim 0$ and 1–2. It should be noted though that the behaviour of the low power FRIs is not thoroughly investigated here, but the evolution seen for higher power objects is consistent with this model.

The detection in this work of FRI space density enhancements for sources with $P_{1.4\text{GHz}} \geq 10^{25}$ W/Hz, along with the previous studies which find essentially luminosity dependent evolution for the FRI population, strongly suggests that neither the intrinsic or the extrinsic difference models can fully explain the observed FRI/II differences. When radio galaxies are divided according to their line luminosities, as in Willott et al. (2001), there are both FRI and FRII sources in the low excitation, low luminosity, population; this implies that these FRIIs may also have inefficient accretion flows similar to those previously proposed for FRIs (e.g. Ghisellini & Celotti 2001). Jets produced by low accretion flow sources are generally weak with the majority having an FRI type structure, whereas higher accretion flows give rise to stronger, mainly FRII type jets. In this scenario therefore, both low and high accretion flows are capable of producing both FR jet structures and the morphological differences between the two classes can be explained extrinsically, as a function of their individual environments, whilst the differences in line luminosity can be explained intrinsically, as a function of their black hole properties (e.g. Hardcastle, Evans & Croston 2006).

In summary, therefore, combining these results with the previously published work in this field leads to the conclusion that the intrinsic/extrinsic models used to describe the differences in radio sources are too simplistic, and that what is needed is some combination of the two. Dividing radio galaxies according to line luminosity, instead of according to their observed morphology, may be the answer as, in this classification, weak, inefficiently accreting, FRIIs can be grouped together with FRIs.

ACKNOWLEDGMENTS

EER acknowledges a research studentship from the UK Particle Physics and Astronomy Research Council. PNB would like to thank the Royal Society for generous financial support through its University Research Fellowship scheme. The VLA is operated by the National Radio Astronomy Observatory, a facility of the National Science Foundation operated under cooperative agreement by Associated Universities Inc. MERLIN is a National Facility operated by the University of Manchester at Jodrell Bank Observatory on behalf of STFC

REFERENCES

- Baum S.A., Zirbel L., O'Dea C. P., 1995, *ApJ*, 451, 88
- Becker R.H., White R.L., Helfand D.J., 1995, *ApJ*, 450, 559
- Best P.N., Röttgering H.J.A., Lehnert M.D., 1999, *MNRAS*, 310, 223
- Best P. N., Kauffmann G., Heckman T. M., Ivezić Ž., 2005, *MNRAS*, 362, 9
- Best P. N., Kaiser C. R., Heckman T. M., Kauffmann G., 2006, *MNRAS*, 368, L67

Bower R. G., Benson A. J., Malbon R., Helly J. C., Frenk C. S., Baugh C. M., Cole S., Lacey C. G., 2006, MNRAS, 370, 645

Clewley L. & Jarvis M., 2004, MNRAS, 352, 909

Condon J.J., Cotton W.D., Greisen E.W., Yin Q.F., Perley R.A., Taylor G.B., Broderick J.J., 1998, AJ, 115, 1693

Diamond P.J., Garrington S.T., Gunn A.G., Leahy J.P., McDonald A., Muxlow T.W.B., Richards A.M.S., Thomasson P. 2003 The MERLIN User Guide

Dunlop J.S. & Peacock J.A., 1990, MNRAS, 247, 19

Fanaroff B.L. and Riley J.M., 1974, MNRAS, 167, 31

Gawroński M. P., Marecki A., Kunert-Bajraszewska M., Kus A. J., 2006, A&A, 447, 63

Gopal-Krishna & Wiita P.J., 2000, A&A, 363, 507

Hardcastle M.J., Evans D.A., Croston J.H. 2006, MNRAS, 370, 1893

Jackson C.A. & Wall J.V., 1999, MNRAS, 304, 160

Jamrozy M., 2004, A&A, 419, 63

Kaiser C.R., Best P.N., 2007, arXiv:0708.3733

Koo D. C. & Kron R. G., 1982, A&A, 105, 107

Kron R. G. 1980, ApJS, 43, 305

Laing R.A., Riley J.M., Longair M.S. 1983, MNRAS, 204, 151

Ledlow M.J. & Owen F.N., 1996, AJ, 112, 9

Muxlow T.W.B., Richards A.M.S., Garrington S.T., Wilkinson P.N., Anderson B., Richards E.A., Axon D.J., Fomalont E.B., Kellermann K.I., Partridge R.B., Windhorst R.A., 2005, MNRAS, 358, 1159

Oort M. J. A. & van Langevelde H. J., 1987, A&AS, 71, 25

Oort M. J. A. & Windhorst R. A., 1985, A&A, 145, 405

Rigby E.E., Snellen I.A.G., Best P.N., 2007, MNRAS, 380, 1449

Sadler E.M., Cannon R.D., Mauch T., Hancock P.J., Wake D.A., Ross N., Croom S.M., Drinkwater M.J., Edge A.C., Eisenstein D., Hopkins A.M., Johnston H.M., Nichol R., Pimbblet K.A., de Propris R., Roseboom I.G., Schneider D.P., Shanks T. 2007, MNRAS, 381, 211

Snellen I. A. G. & Best P. N., 2001, MNRAS., 328, 897

Snellen I. A. G., Bremer M. N., Schilizzi R. T., Miley G. K., van Ojik R., 1996, MNRAS, 279, 1294

Stoughton C. et al., 2002, AJ, 123, 485

Waddington I., Windhorst R.A., Dunlop J.S., Koo D.C., Peacock J.A., 2000, MNRAS, 317, 801

Waddington I., Dunlop J.S., Peacock J.A., Windhorst R.A., 2001, MNRAS, 328, 882

Wall J.V., 1980, Phil. Trans. R. Soc., A296, 367

Willott C.J., Rawlings S., Blundell K.M., Lacy M., Eales S.A., 2001, MNRAS., 322, 536

Willott C. J., Rawlings S., Jarvis M. J., Blundell K. M., 2003, MNRAS, 339, 173

Windhorst R.A., van Heerde G.M., Katgert P., 1984, A&AS, 58, 1

York D.G. et al., 2000, AJ, 120, 1579

This paper has been typeset from a \TeX / \LaTeX file prepared by the author.

APPENDIX A: LYNX B-ARRAY RADIO IMAGES

APPENDIX B: COMPLETE RADIO IMAGES FOR SOURCES INCLUDED IN THE HIGH-RESOLUTION OBSERVATIONS

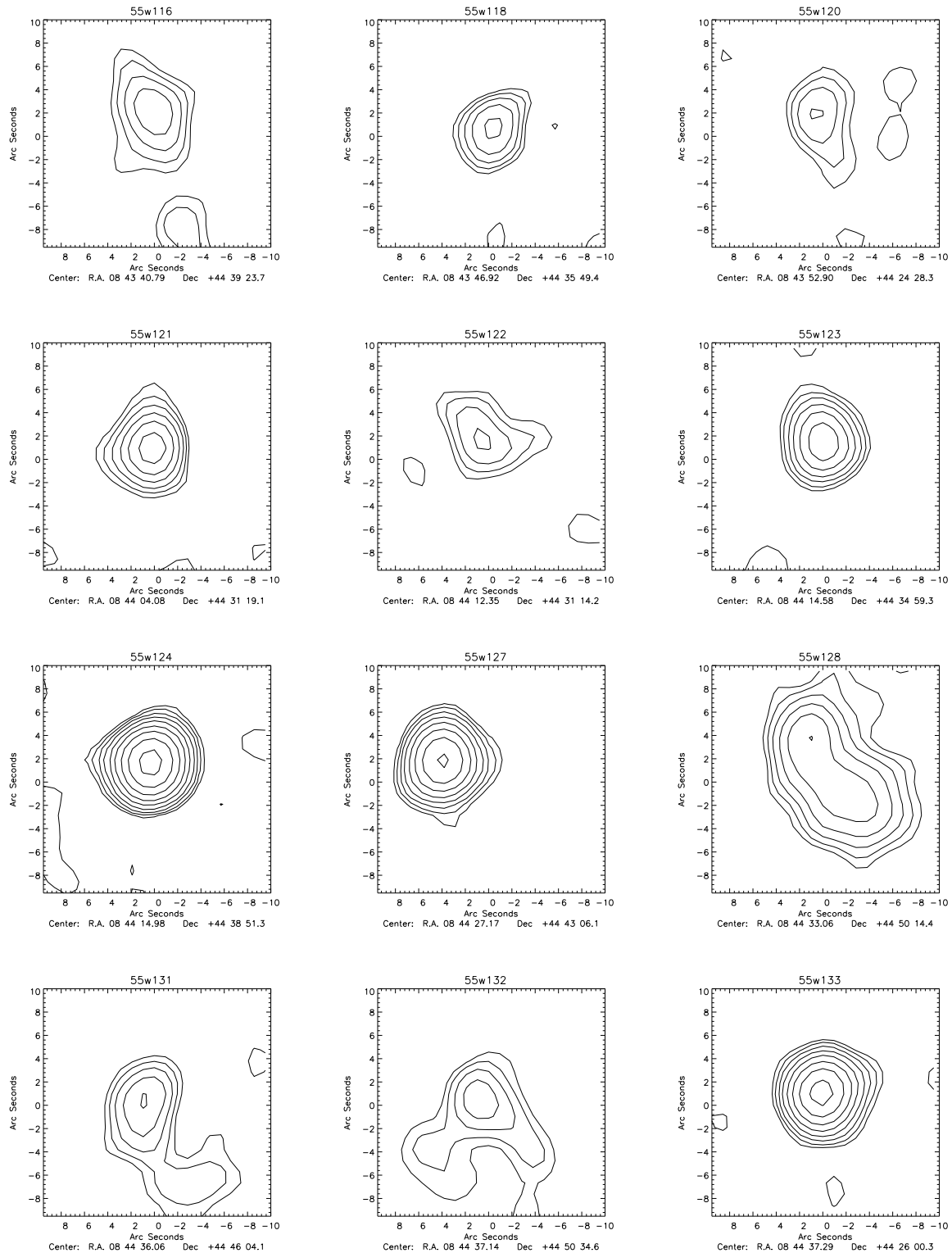


Figure A1. The radio contour images, for the Lynx field complete sample, from the VLA 1.4GHz B–array observations. The beam size is $5.36'' \times 4.67''$. Contours start at $50\mu\text{Jy}/\text{beam}$ and are separated by factors of $\sqrt{2}$. The images are centred on the optical host galaxy positions from Paper I if available.

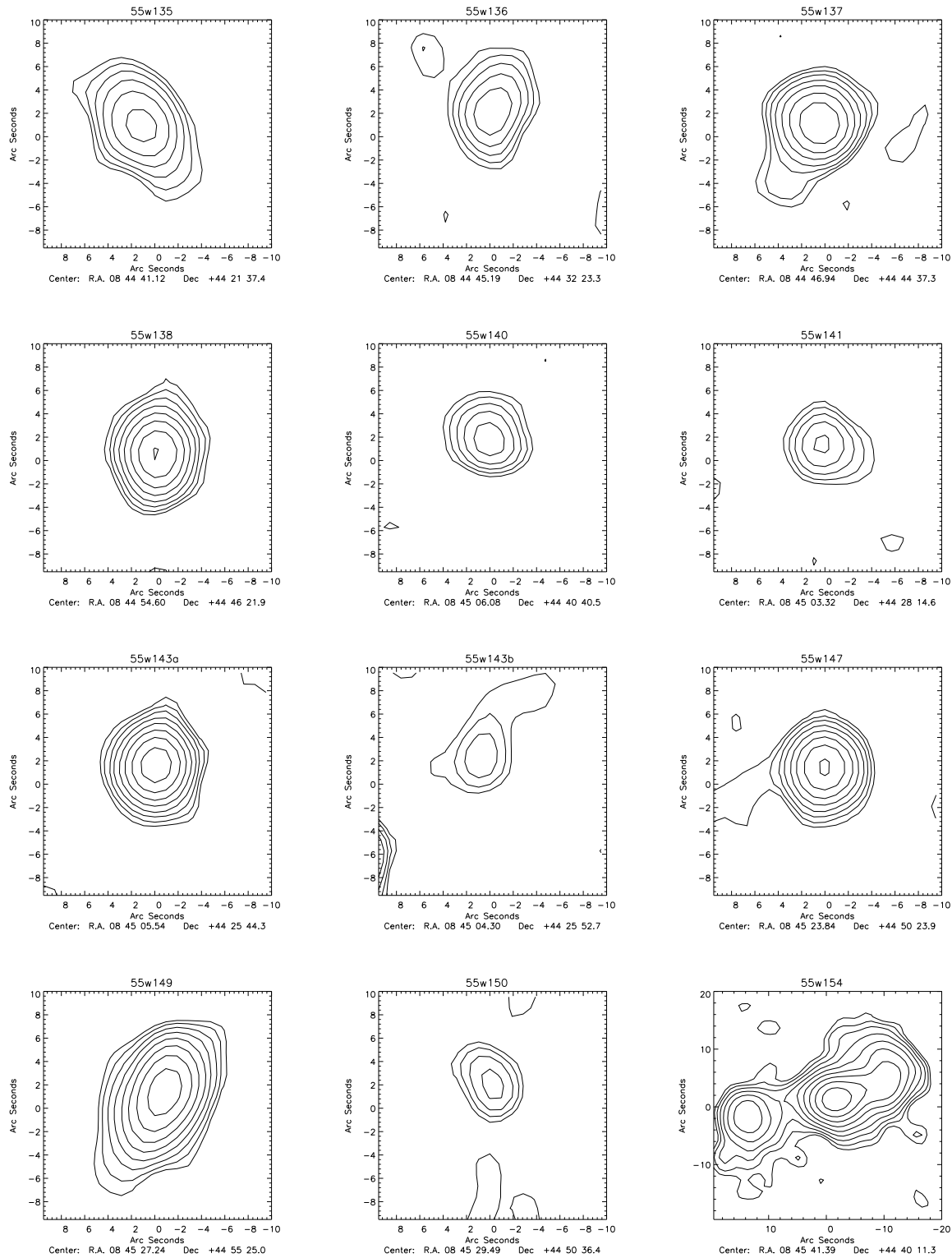


Figure A1 – continued

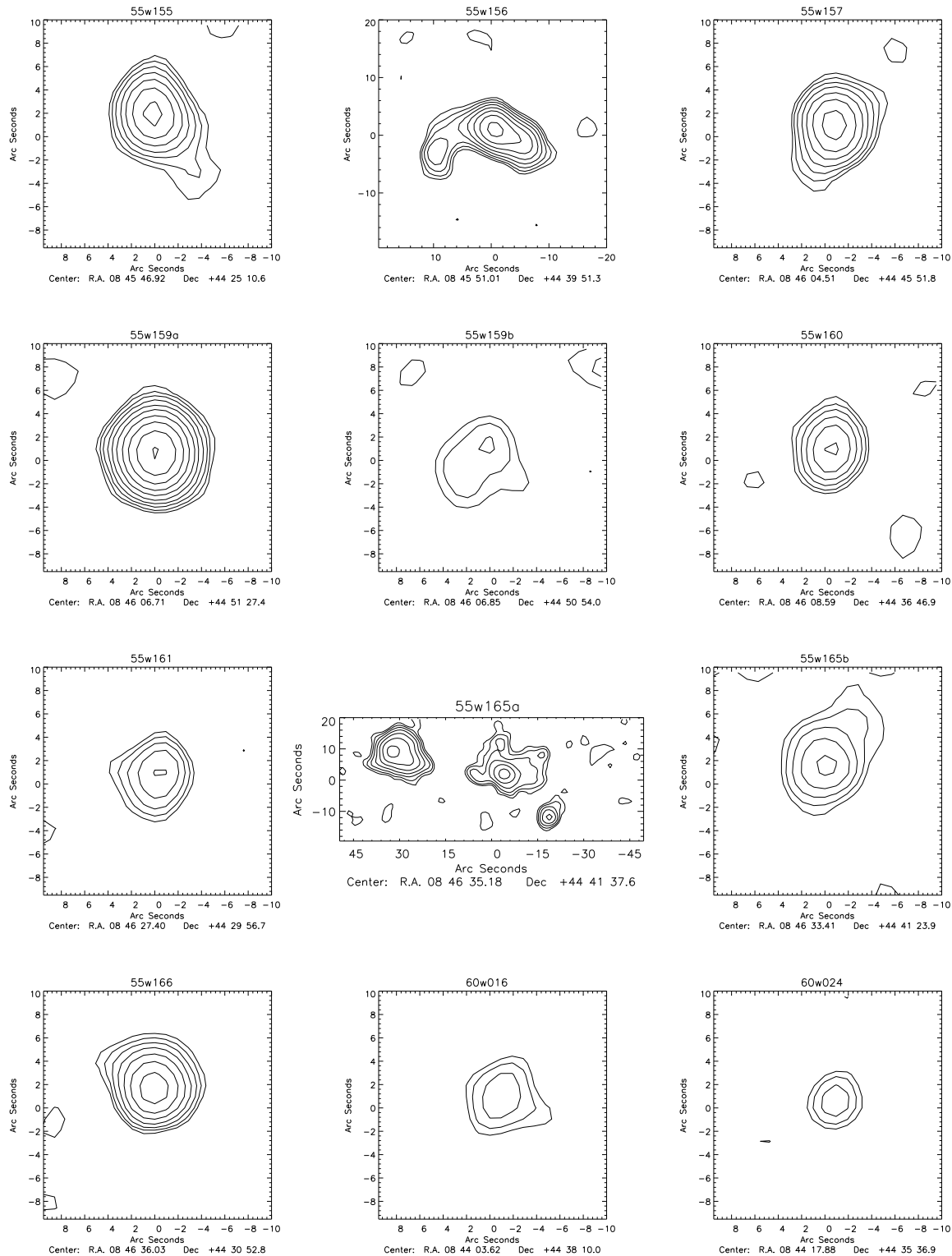


Figure A1 – continued

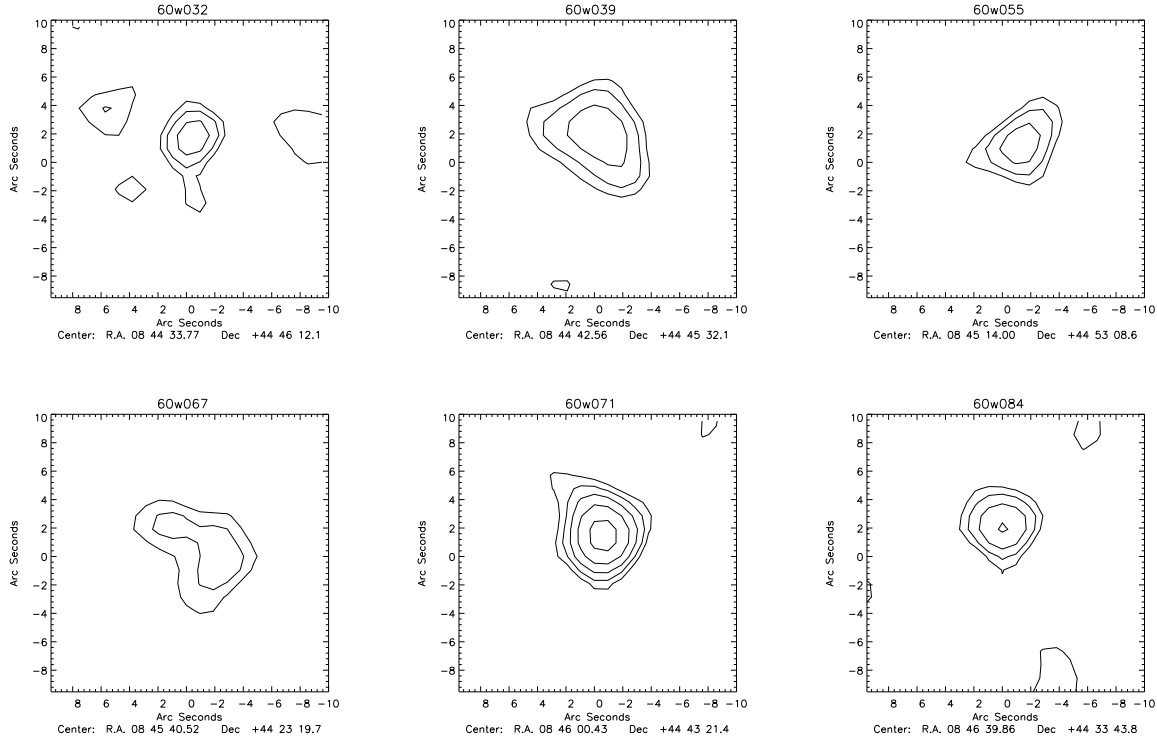


Figure A1 – continued

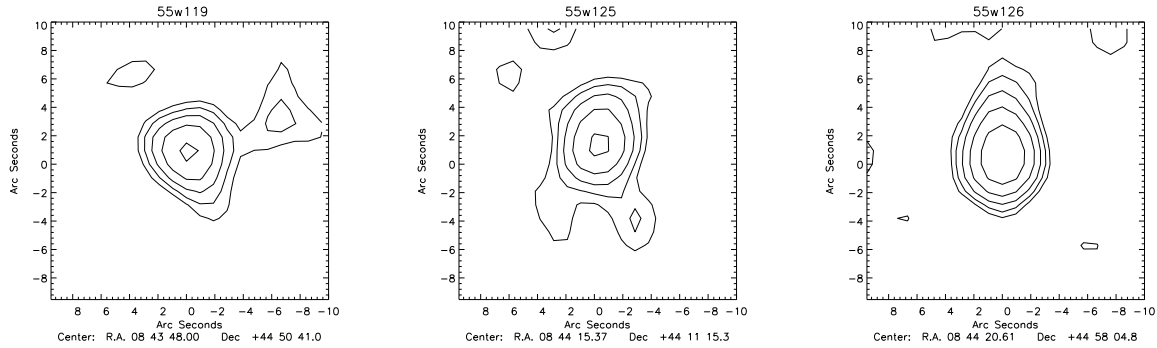


Figure A2. The B–array radio contour images, for the sources not included in the Lynx field complete sample. The beam size is $5.4'' \times 4.5''$. Contours start at $50 \mu\text{Jy}/\text{beam}$ and are separated by factors of $\sqrt{2}$. The images are centred on the optical host galaxy positions from Paper I if available.

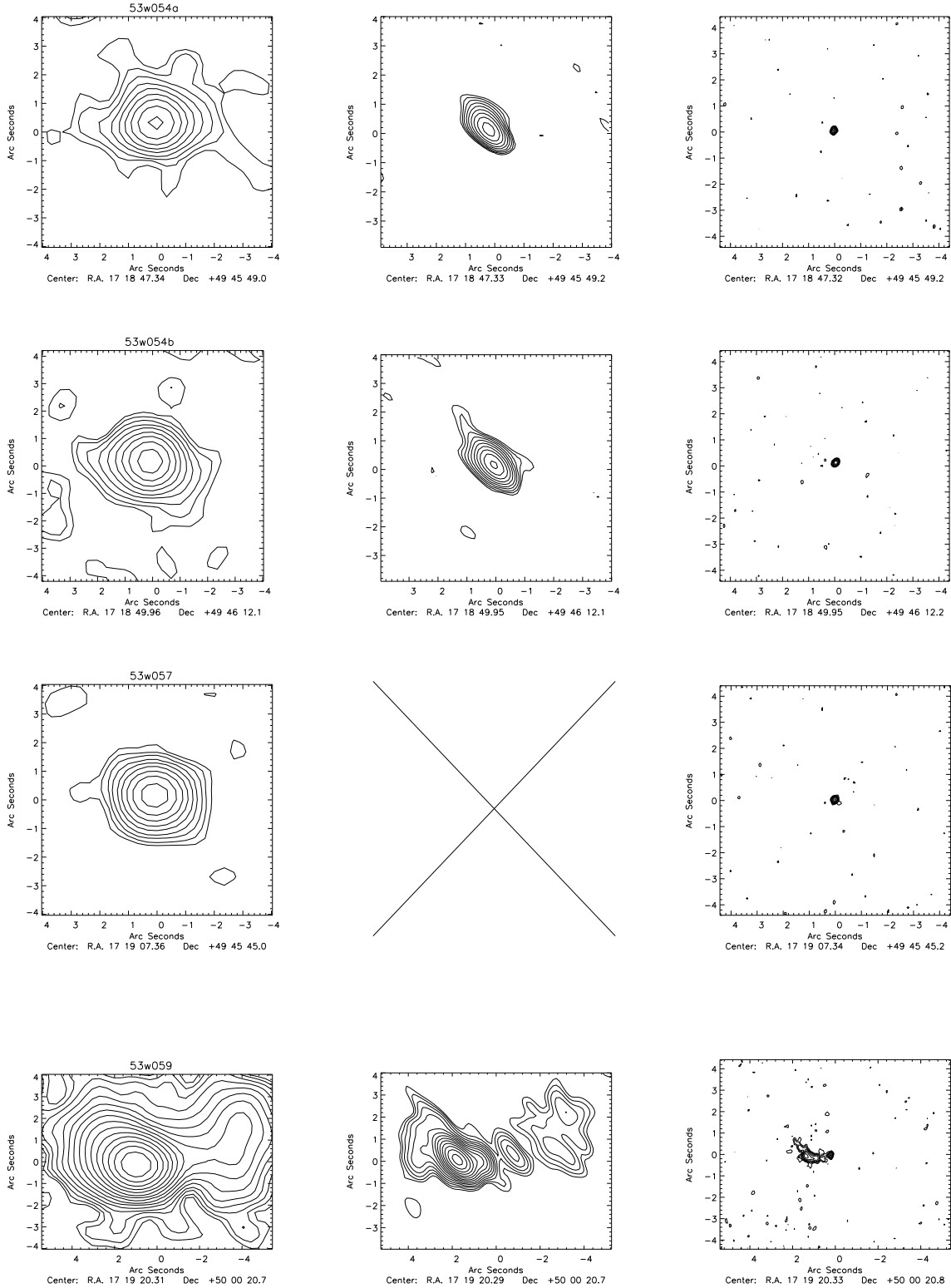
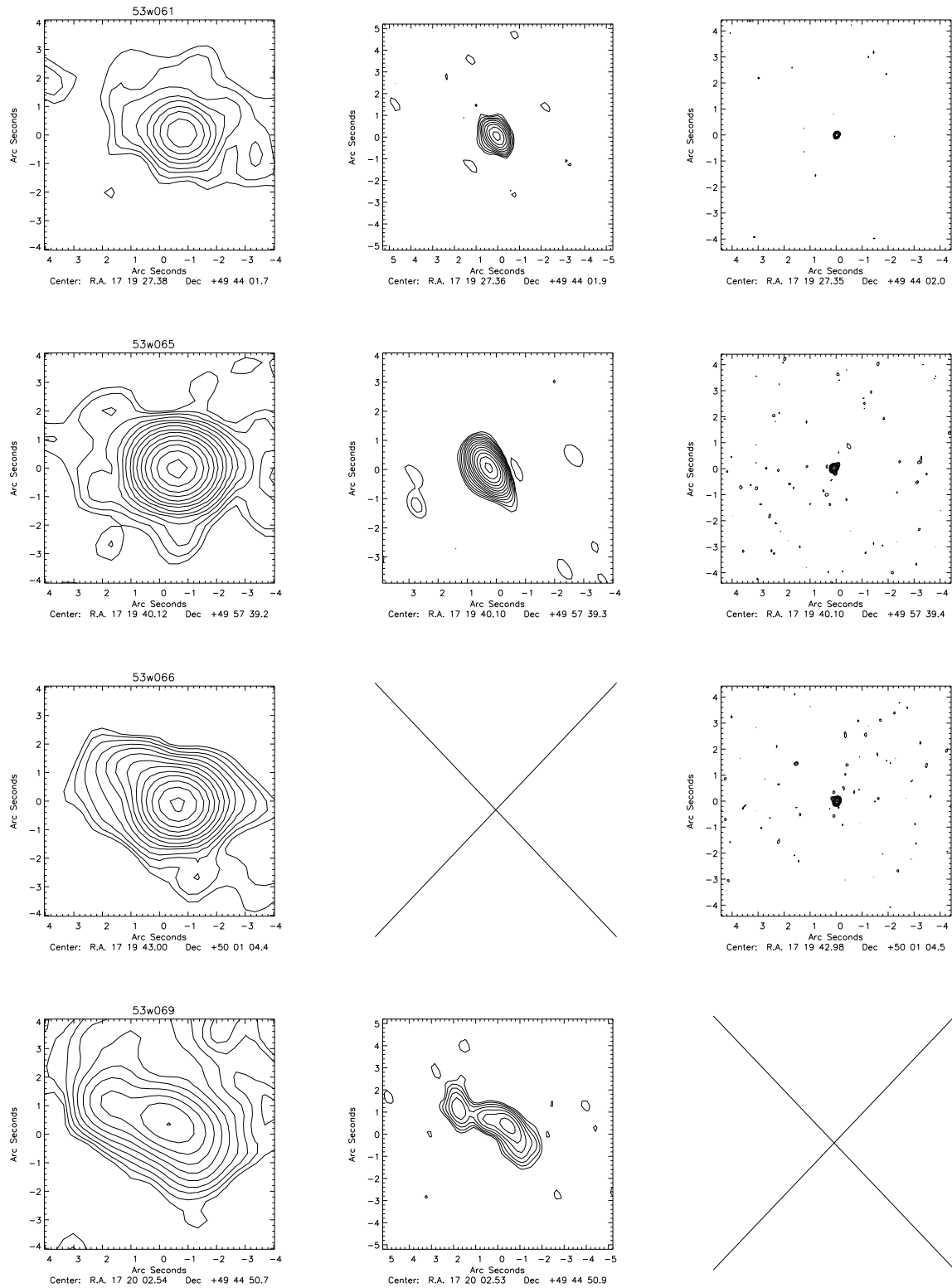


Figure B1. The A-array, A+Pt and MERLIN contour maps for the sources in the Hercules field, included in the A+Pt or MERLIN observations, all centred on the optical host galaxy position if available, with the aim of comparing the source morphologies at the three different resolutions, $\sim 1.5''$ $\sim 0.5''$ and $\sim 0.18''$. The contour maps for each source are all of equal size and all contours increase by a factor of $\sqrt{2}$.



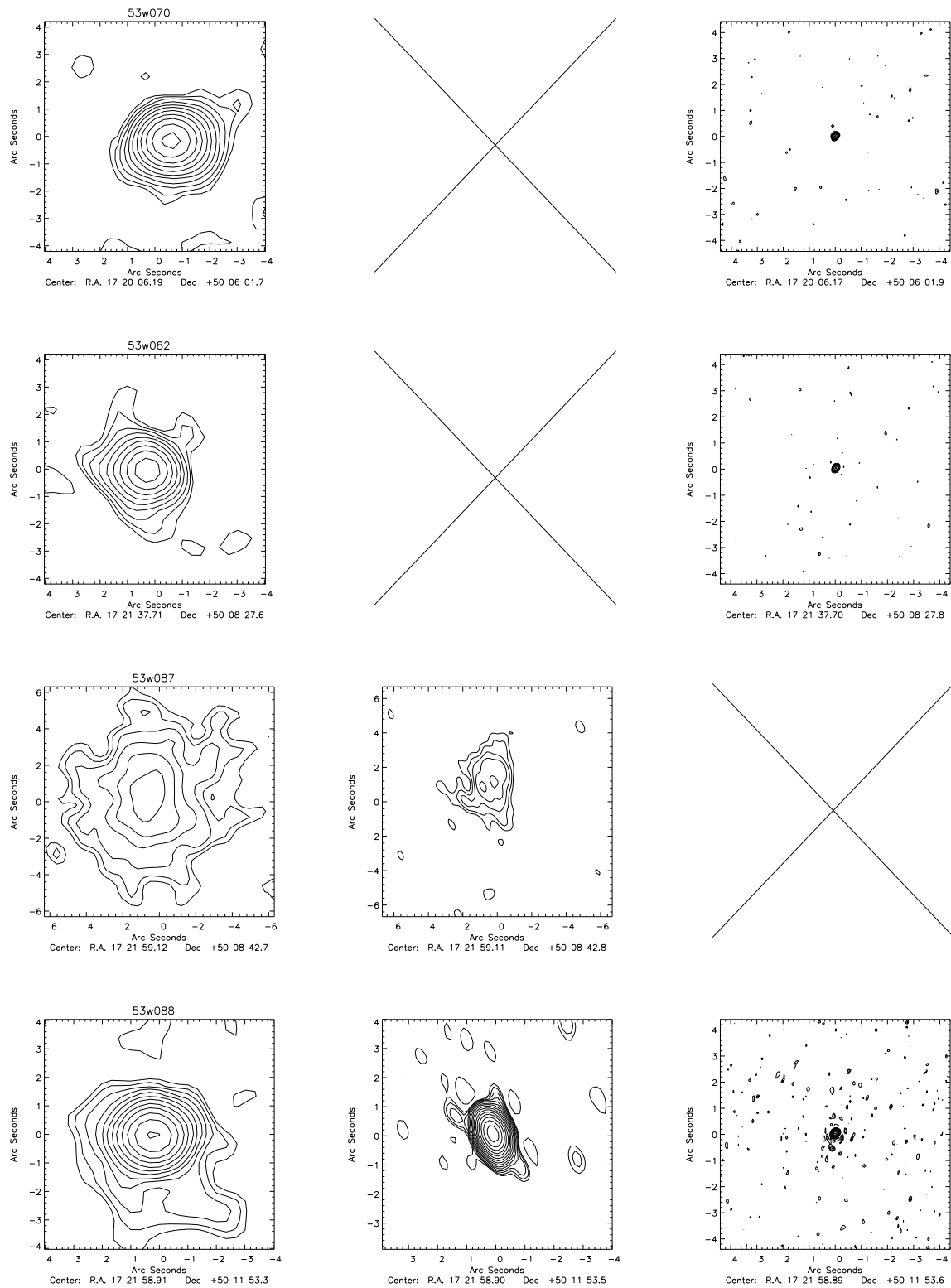


Figure B1 – continued

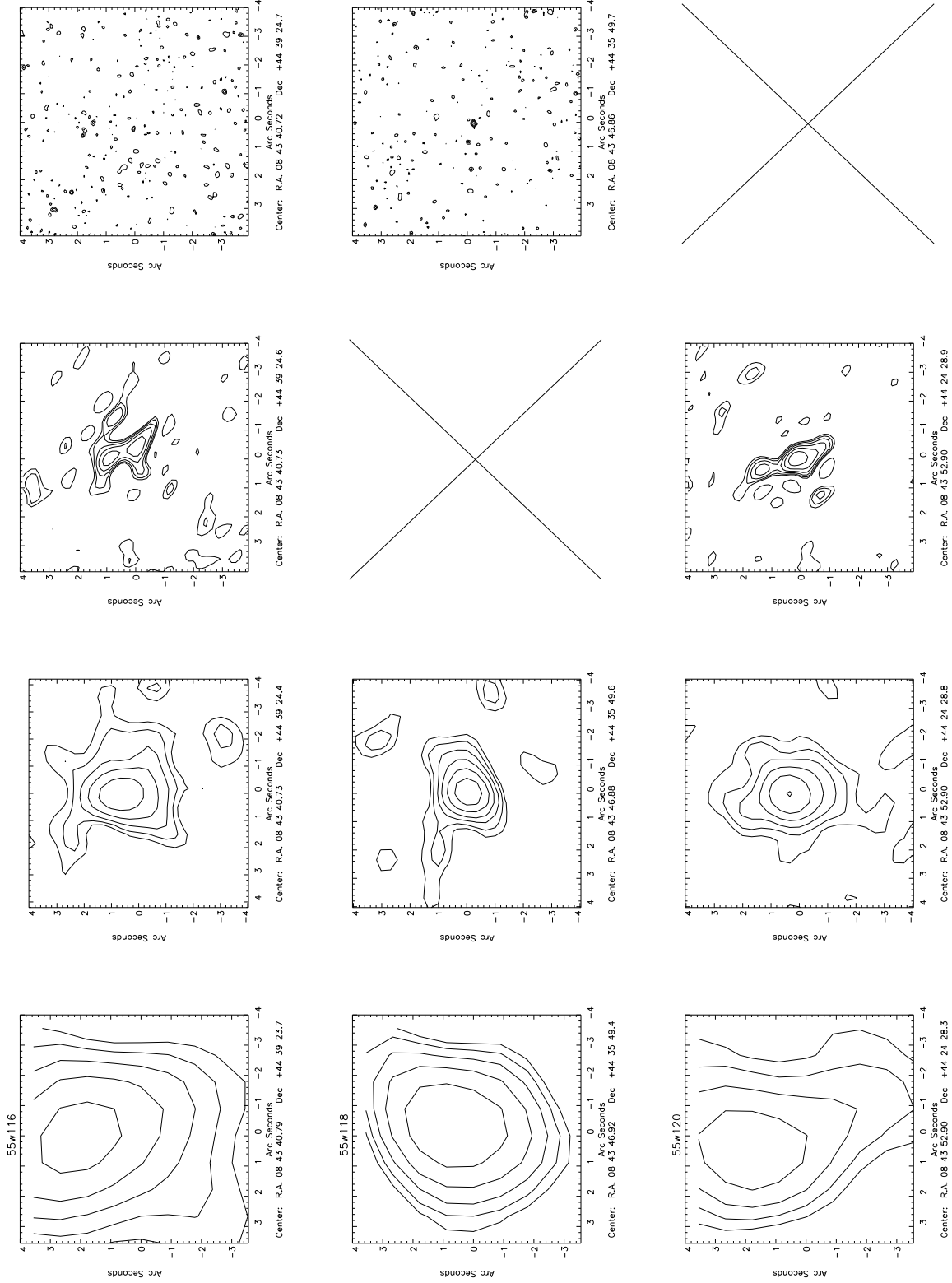


Figure B2. (landscape) The B–array, A–array, A+Pt and MERLIN contour maps for the sources in the Lynx field, included in the A+Pt or MERLIN observations, all centred on the optical host galaxy position if available, with the aim of comparing the source morphologies at the four different resolutions, $\sim 5''$, $\sim 1.5''$, $\sim 0.5''$ and $\sim 0.18''$. The contour maps for each source are all of equal size and all contours increase by a factor of $\sqrt{2}$.

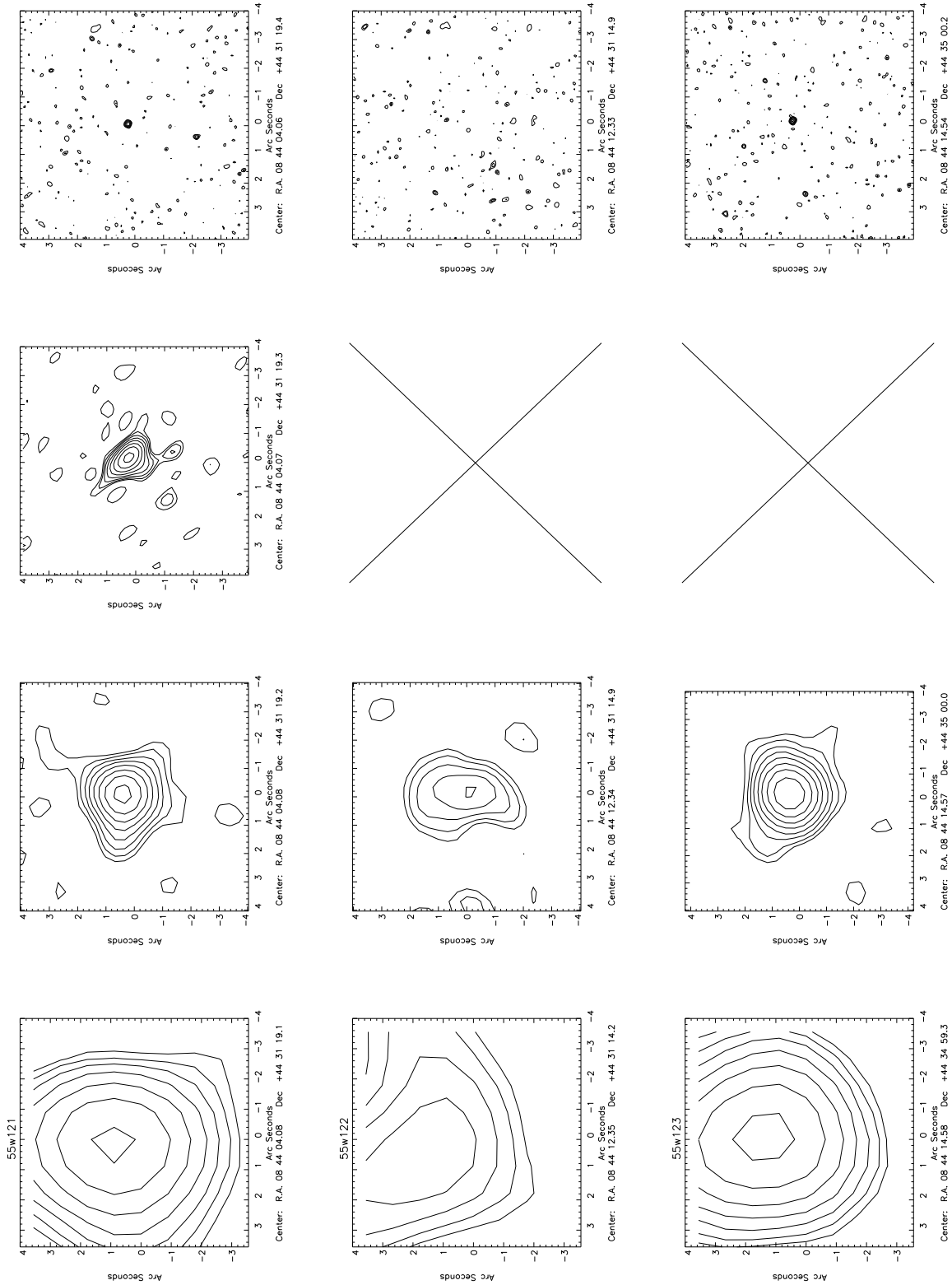


Figure B2 – continued

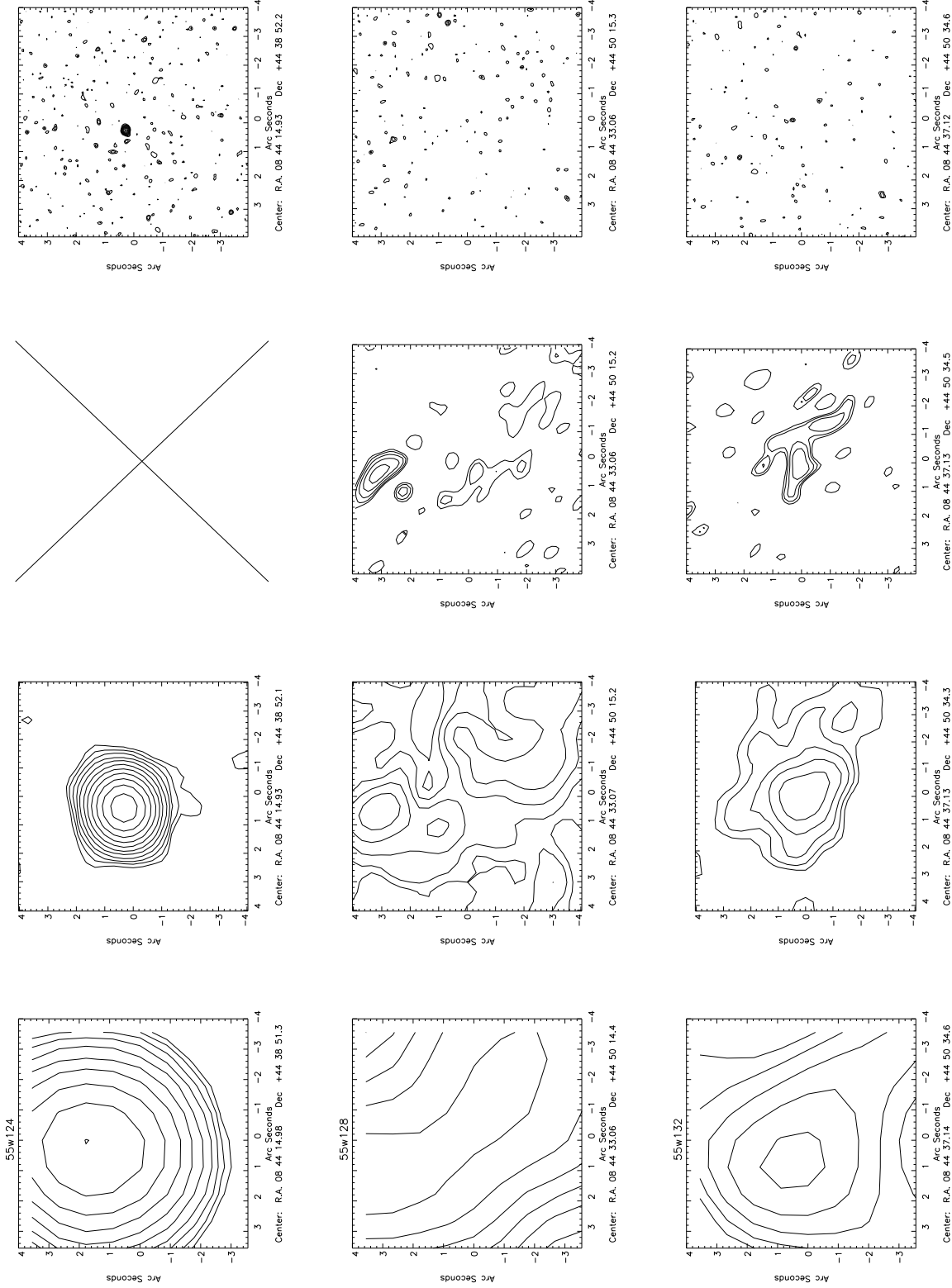


Figure B2 – continued

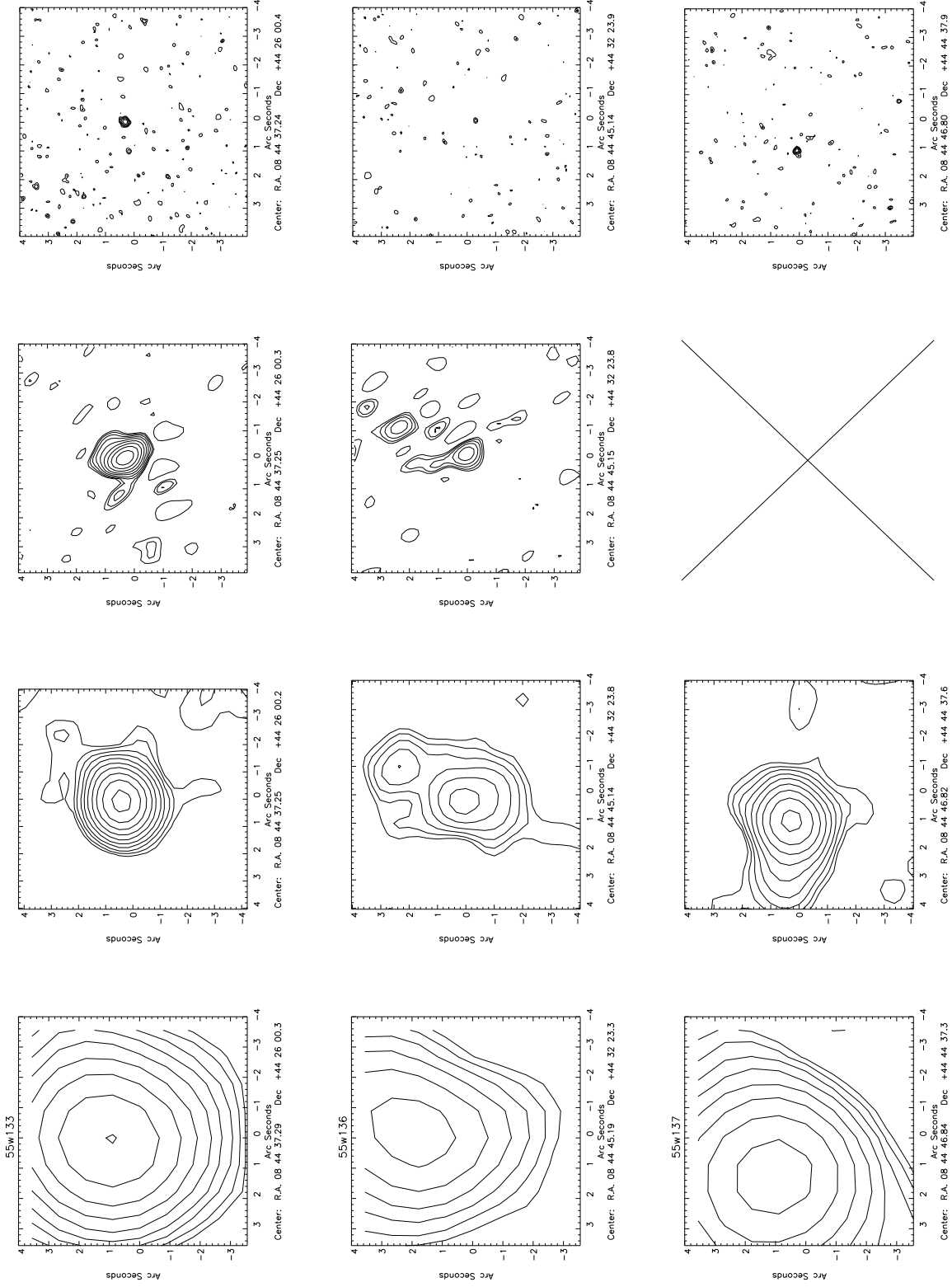


Figure B2 – continued

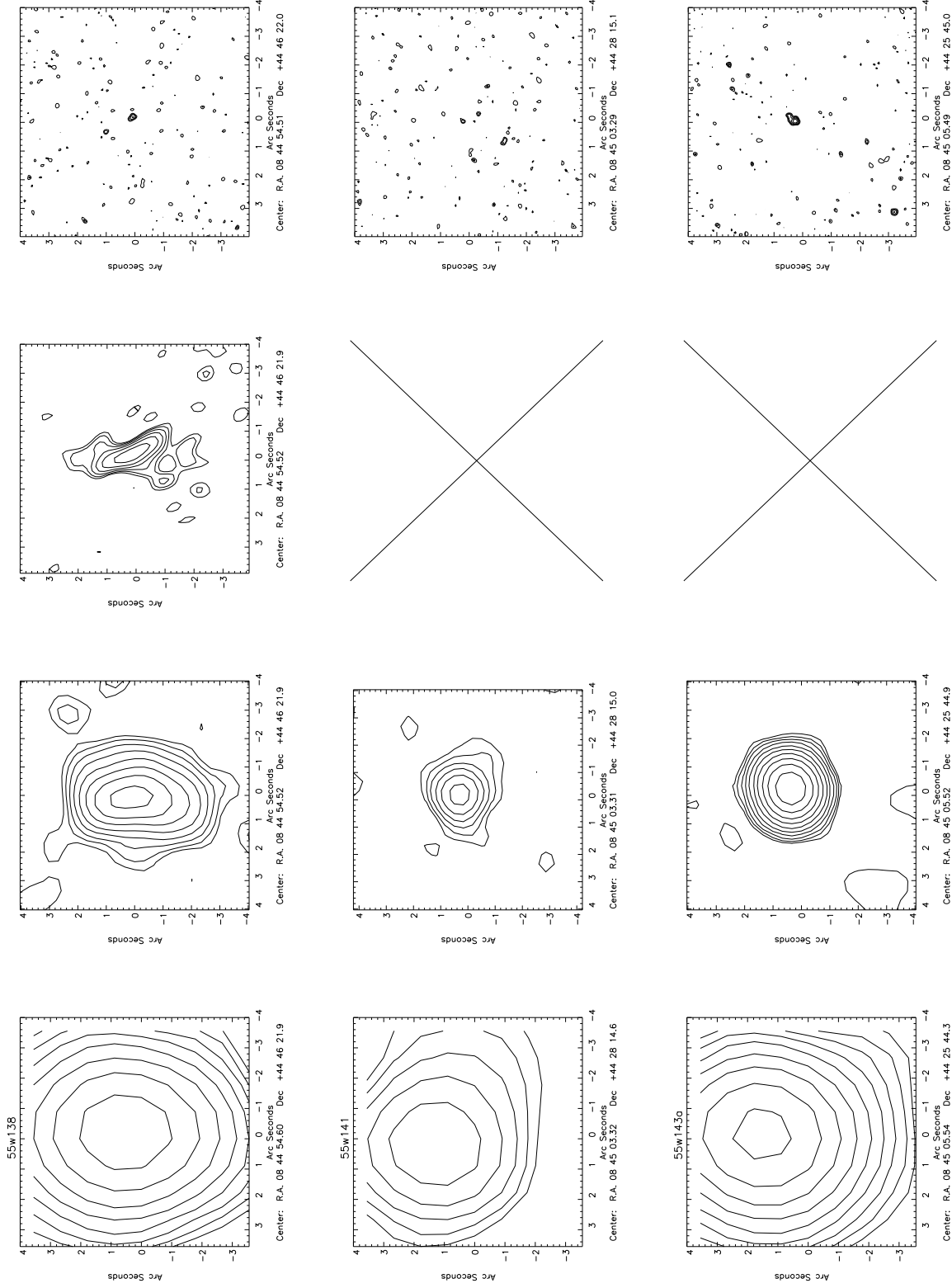


Figure B2 – continued

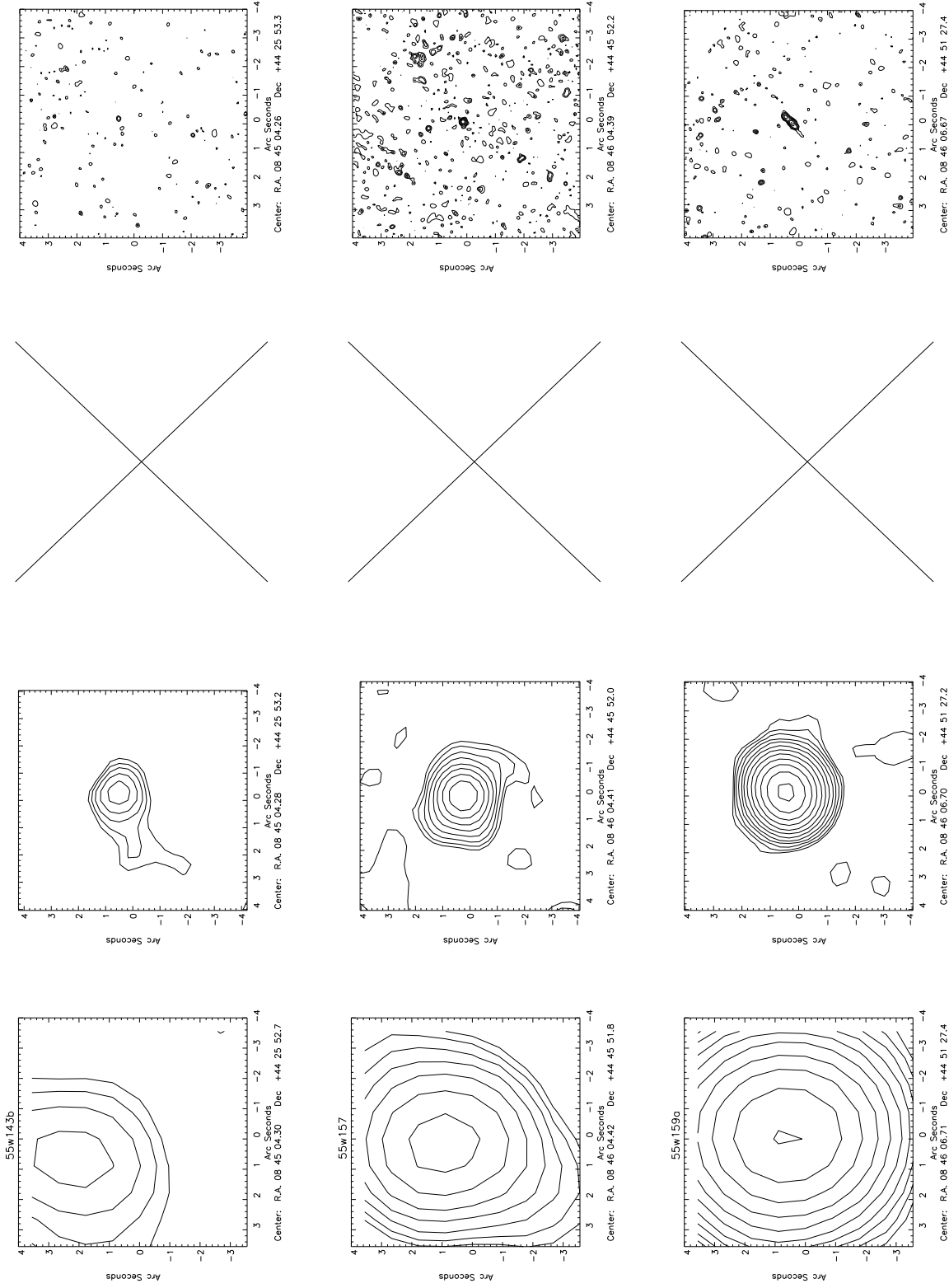


Figure B2 – continued

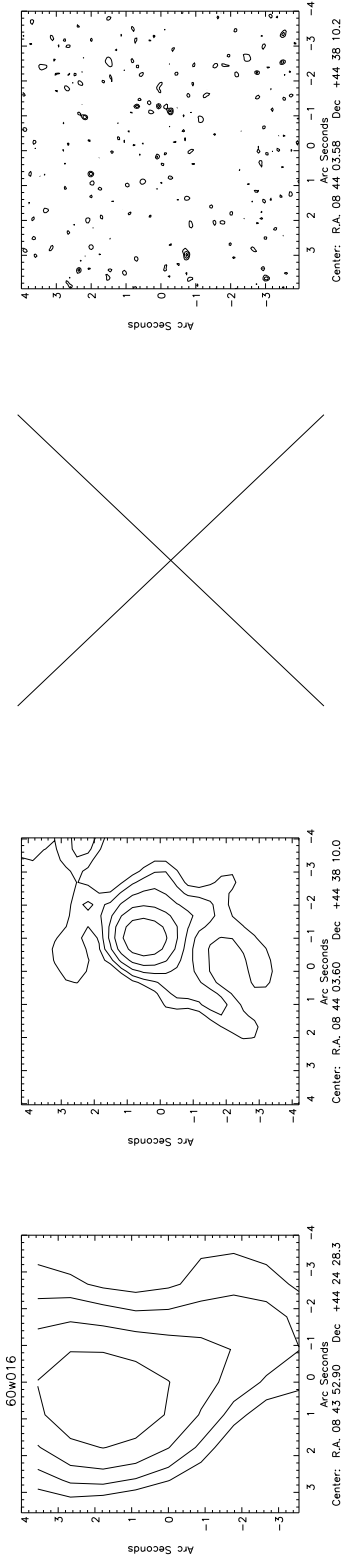


Figure B2 – *continued*